

Analyse turbulent flows via Empirical Mode Decomposition

Analyse turbulenter Strömungen
mittels Empirical Mode Decomposition

Master Thesis of

Marion Cormier

At the Department of Mechanical Engineering,
Institute of Fluid Mechanics

Advisors: Prof. Dr.-Ing. Bettina Frohnnapfel
Dr.-Ing. Davide Gatti

Duration: January 2016 – Mai 2016

I declare that I have developed and written the enclosed thesis completely by myself, and have not used sources or means without declaration in the text.

Karlsruhe, 10. 05. 2016

.....
(Marion Cormier)

Contents

Abstract	1
1. Introduction	2
2. Fundamentals	4
2.1. High Reynolds number turbulence in channel flows	4
2.1.1. Turbulence in channel flows	4
2.1.2. Turbulent coherent structures	5
Very large scale motions	6
Influence of turbulent superstructures on the flow field	7
Extraction of the superstructures from a turbulent flow field	8
2.2. Drag reduction strategies in wall-bounded turbulent flows	10
2.2.1. Definition of drag reduction	10
2.2.2. Classification of flow-control strategies	10
2.2.3. Streamwise traveling waves of spanwise wall velocity	10
2.3. Empirical Mode Decomposition (EMD)	11
3. Empirical mode decomposition for scale separation of 2D-streamwise velocity signals	15
3.1. Preliminary transformations of the flow field	15
3.2. Bidimensional scale separation algorithm	16
3.2.1. Fast and adaptive bisimensional empirical mode decomposition	16
Envelope estimation based on order-statistics filters	17
Algorithm of the FABEMD	18
3.2.2. FABEMD vs. BEMD	18
4. Response of VLSM to wall-based friction drag reduction	22
4.1. Preliminary study of the FABEMD window-sizing method w	22
4.1.1. The narrow-window methods	23
4.1.2. The large-window methods	24
4.1.3. Narrow-window vs. large-window methods	25
4.1.4. Results	27
4.2. Scale decomposition of controlled and uncontrolled flows	28
4.2.1. Turbulent superstructures captured	28
4.2.2. Premultiplied energy spectra	28
4.2.3. Cross-correlations of the fluctuations across the flow height	29
Small-scale fluctuations	29
Large-scale fluctuations	29
4.3. Correlation of the friction velocity with the VLSM fluctuations	31
4.4. Concluding discussion	34
5. Conclusion	36

Symbols and Abbreviations	38
List of Figures	39
List of Tables	41
Bibliography	42
Appendix	45
A. Data processing : from (v, η) to (u, v, w)	45
B. FABEMD: Lena picture decomposition with the 4 window-sizing methods .	45

Abstract

Effects of wall-based skin-friction drag reduction strategies on the statistical properties of large-scale motions in moderate-Reynolds number turbulent flows have been investigated by exploiting Direct Numerical Simulation of turbulent channels. To educe large scales, a new efficient parallel distributed memory algorithm has been implemented which delivers data-driven modes of increasing characteristic lengthscales: the fast and adaptive bidimensional Empirical Mode Decomposition (EMD). By varying a decisive parameter in this algorithm, different methods have been defined to perform the scale separation. An analysis of the properties featured by the signals obtained via these different methods led to the determination of a systematic algorithm to extract large-scale motions of turbulent channels. To investigate the influence of wall-based skin friction reduction, large scales of controlled and uncontrolled channel flow fields at constant friction Reynolds number have been statistically analyzed via observing energy levels and velocity cross-correlations. A spatial reorganization of the turbulent superstructures and a global decrease of the energy levels in controlled flows have been found. The traditional way of observing footprinting, as cross-correlation of the streamwise velocity components at different wall-distances, has been found to be unreliable when comparing drag-reduced flows, due to the arbitrary choice of a reference plane in the logarithmic layer. A more sound way of observing the footprinting via the correlation of the streamwise velocity with the friction velocity is addressed and shows an increase of the footprinting in drag-reduced flows.

1. Introduction

The increasing concerns about reducing the energy needs, with important economical and environmental consequences, prompts the development of flow control strategies aimed at reducing skin-friction drag in transport processes. Since most flows occurring in industrial processes are turbulent, hence characterized by a larger skin-friction drag for a given value of the Reynolds number compared to laminar flows, reducing skin-friction drag in turbulent flows becomes particularly appealing.

Drag reduction strategies have actually been widely investigated over the past decades and successful skin-friction control devices have been developed. The most successful strategies take place at the wall, and feature drag reduction up to 50% at low-Reynolds numbers. The incredible success of wall-based drag reduction strategies finds origins in its proximity to the near-wall turbulence regeneration cycle [11], an important process for the turbulence generation and self-sustainment that takes place in the vicinity of the wall. The main protagonists of this process are small turbulent structures, which appear randomly but repeatedly and feature similar properties: the near-wall quasi-streamwise vortices. They can be directly accessed by the control, which aims at hindering this process.

With increasing Reynolds number, these strategies are known to exhibit decreasing performances [6]. It is conjectured, among other reasons, to be partly caused by the presence of some large-scale structures, residing further away from the wall, at high Reynolds number: the so-called turbulent superstructures. Figure 1.1 highlights the apparition of such structures with increasing Reynolds number, while the viscous lengthscale, characteristic lengthscale of the near-wall vortices, decreases.

According to the modern theory of turbulence, turbulent superstructures feature random, repeated flow structures of similar properties, that have a statistical spatial or temporal persistence and cause strong large-scale turbulent fluctuations [10]. They are assumed to be of major importance in the dynamics of turbulent flows and responsible for a large part in the Reynolds stresses [7]. Although plethora of studies have been consecrated to these meandering structures, no clear-cut definition has yet been acted. In most cases, they have been recognized from the flow field by filtering the wavelengths of the streamwise velocity, with resort to an arbitrary threshold to separate spatial small-scale and large-scale structures.

This study aims at investigating the effects of wall-based friction control on the turbulent superstructures, based on an extraction of the large-scale motions of turbulent flows via empirical mode decomposition. This method allows actually to separate small-scale and

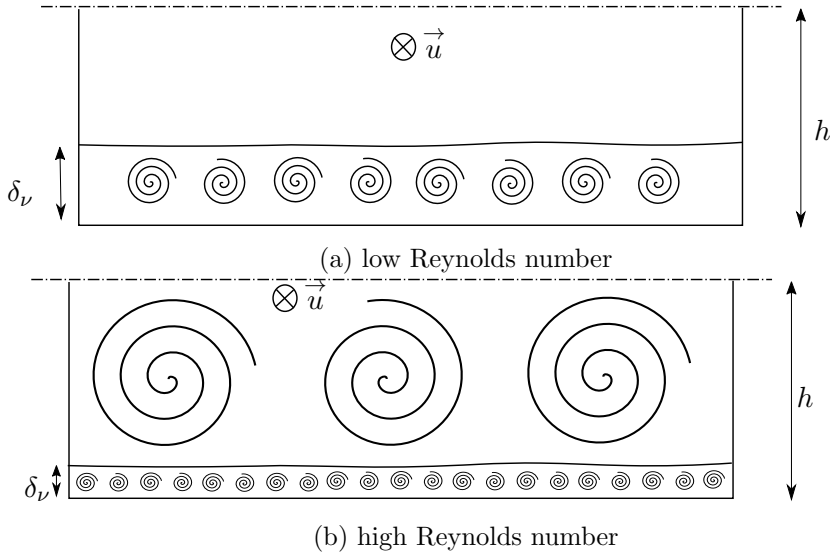


Figure 1.1.: Appearance of turbulent superstructures in a channel flow with increasing Reynolds number

large-scale structures without resorting to any arbitrary threshold [2]. The scale decomposition is performed on a data set of turbulent channel flows at moderate Reynolds number, some of them being provided with an active flow control strategy to reduce the turbulent drag, the so-called streamwise traveling waves of spanwise wall velocity. Statistical observations of the captured small-scale and large-scale motions are examined, in order to describe their properties and the behavior of the large-scale structures under drag-reduced conditions. The results of this work aim at aiding the understanding of the physics behind skin-friction drag reduction at moderate Reynolds number, which is of paramount importance to design and conceive the flow-control strategies of the future.

In the first part, some fundamentals of turbulent channel flows and of flow controls aimed at drag reduction are presented, as well as Huang's empirical mode decomposition theory. In the second part, the implemented bidimensional empirical mode decomposition aiming at separating the scales of turbulent channel flows is presented. Finally, a systematical way to perform scale separation of turbulent flows is outlined and the results obtained on controlled and uncontrolled channel flow fields are presented. The response of the flow to the wall-based control device is examined via statistical observations.

2. Fundamentals

The present work has two main goals: the first one consisting in implementing a code separating the large scale and the small scale components of a signal, and the second one consisting in applying it on a fully developed turbulent channel flow and analyzing the results. This aims at extracting the very large scale motions (VLSM) of turbulent channel flows, in order to study the effects of wall-bounded skin-friction drag reduction strategies on them.

In this chapter, the main characteristics of turbulent flows in channels is first described. Then, the appearance and effect of turbulent superstructures in high Reynolds number flows is briefly introduced. Flow-control strategies aimed at reducing skin-friction drag in turbulent flows are presented, with particular focus on the control strategy of interest for the present work: the streamwise-travelling waves of spanwise wall velocity. Finally, the empirical mode decomposition, a data-driven signal decomposition method, is described.

2.1. High Reynolds number turbulence in channel flows

Turbulent channel flows are highly investigated as they represent a simplification of wall-bounded flows, which are present in many practical cases. This part aims at defining turbulent channel flows, and introducing the turbulent superstructures, characteristic meandering motions of high Reynolds numbers flows.

2.1.1. Turbulence in channel flows

As represented on figure 2.1, a turbulent flow seeps through a rectangular section of size $L_x = 4\pi h$, $L_y = 2h$ and $L_z = 2\pi h$, delimited by an upper and a lower wall. The velocity vector in the coordinates system (x, y, z) is defined as (u, v, w) , and the main stream direction is the x -direction.

As the channel presents a large aspect ratio $L_z/h \gg 1$, the flow is statistically independent in the z -direction. It is also long, $L_x/h \gg 1$, and at high enough Reynolds numbers two main regions can be defined in the x -direction: near the entrance, a flow development region contains non-stationary velocity components, and at large x , a fully developed flow is statistically stationary and homogeneous in the streamwise direction. Fully developed turbulent flows are thus statistically stationary and homogeneous in the streamwise and spanwise directions:

$$\bar{u} = \langle u \rangle_{x,z,t} \quad (2.1)$$

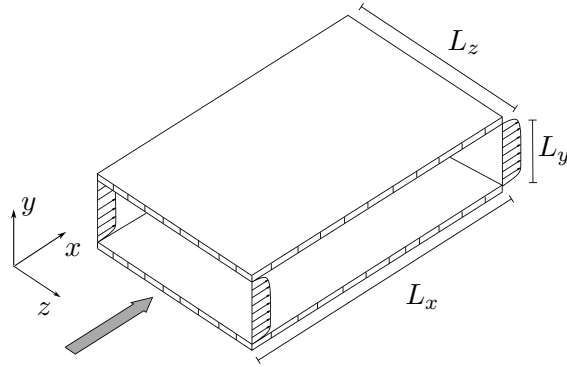


Figure 2.1.: Channel flow geometry

To satisfy the homogeneity condition in x- and z-directions in numerical simulations, a periodicity condition is set in those directions.

Turbulent flows are characterized by their Reynolds number

$$\text{Re} = \frac{\bar{U}2h}{\nu} \quad (2.2)$$

with $\bar{U} = \frac{1}{h} \int_0^h \langle u \rangle dy$ the bulk velocity, defined as the mean velocity that crosses a section perpendicular to the wall and ν the kinematic viscosity of the fluid.

Two flows having the same Reynolds number at constant volume flow rate $Q = \bar{U}L_z h$ are said to be similar. If instead of Q the mean pressure drop is constant $\frac{\partial \langle p \rangle}{\partial x} = \frac{dp_w}{dx}$, two similar flows will not have the same Re but the same Reynolds friction number

$$\text{Re}_\tau = \frac{u_\tau h}{\nu} \quad (2.3)$$

with $u_\tau = \sqrt{\tau_w/\rho}$ the friction velocity, defined in function of the wall shear-stress $\tau_w = -\frac{dp_w}{dx}h$ and the density of the fluid ρ . One can remark that Re_τ represents the dimensionless semi-height of the channel h , and thus the relative importance of viscous length and channel height.

From now on, only the case with a constant pressure gradient is considered, as it is the one studied in the following. In this case, the lengths scale with the viscous lengthscale ν/u_τ and the velocities with the friction velocity u_τ .

The dimensionless quantities are noted with an exponent $+$. Applied to the wall-normal distance y , it yields to

$$y^+ = \frac{yu_\tau}{\nu} \quad (2.4)$$

According to the value taken by the normalized wall-distance y^+ , it is used to define different regions of the flow, as sketched in figure 2.2, which feature specific behaviors. The viscous wall region refers to the vicinity of the wall, which is dominated by the viscous forces, and defined up to $y^+ = 50$. It is contained in the inner layer, in which the mean velocity is determined by the friction velocity. The outer layer refers to a further region, from $y^+ > 50$, in which the direct effects of viscosity are negligible.

2.1.2. Turbulent coherent structures

In spite of the unsteady and apparently chaotic nature of turbulent flows, flow visualizations have shown that they are populated with some characteristic features, which appear

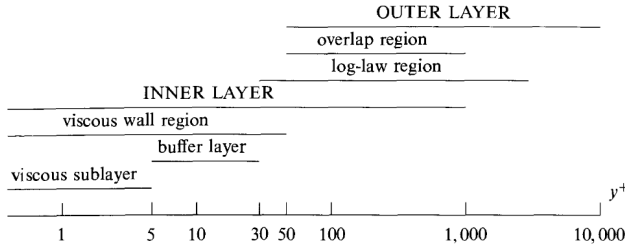


Figure 2.2.: The various wall-regions of turbulent channel flows in function of y^+ at high Reynolds number $Re_\tau = 10^4$ [17]

randomly but regularly in the flow. These features are usually referred to as coherent turbulent structures, because they typically occur with strong temporal or spatial coherence. A key feature of the coherent structures is their implication in the properties of the flow. For example the small-scale turbulence observed in the near-wall region of turbulent flows, and referred as near-wall quasi-streamwise vortices, has been shown to be of paramount importance in the turbulence generation process: the turbulence generation cycle [11].

Depending on the Reynolds number and the flow geometry, other categories of coherent structures can be defined [19]. This section aims at describing a particular kind of coherent structures, the large-scale motions in the outer layer, which appear at moderate to high Reynolds numbers and have been shown to play a key role in the turbulent flow dynamics.

Very large scale motions

It has been seen in equation 2.3 that, in turbulent channel flows, the friction Reynolds number represents the semi-height of the channel h scaled by the viscous length $\delta_\nu = \frac{v}{u_\tau}$, i.e. the ratio of viscous length and channel height. It follows that with the increase of the Reynolds number, the near-wall quasi-streamwise vortices - which scale with δ_ν - become smaller and smaller. As represented in the sketch figure 2.3, the slimming of the viscous boundary layer is accompanied by the appearance of large-scale velocity fluctuations in the outer layer: the so-called very large scale motions (VLSM), or turbulent superstructures.

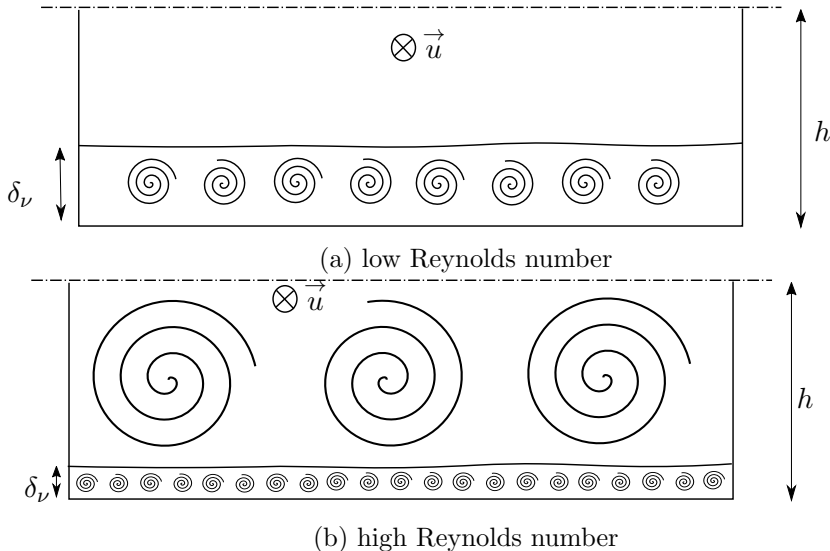


Figure 2.3.: Appearance of turbulent superstructures in a channel flow with increasing Reynolds number

These motions feature characteristic lengthscales of many times the boundary layer thickness and have been shown to meander mainly in the streamwise and spanwise directions

[10].

Influence of turbulent superstructures on the flow field

Turbulent structures present similar properties, which appear especially through the amount of energy they transport. Evolving at high velocities, they feature an increasing turbulence intensity with increasing Reynolds number, given in the streamwise direction by

$$k_x = \frac{\langle u^2 \rangle_{x,z,t}}{u_\tau^2} = \langle (u^+)^2 \rangle_{x,z,t} \quad (2.5)$$

Figure 2.4 highlights the apparition of the corresponding so-called outer peak in the outer layer, which testifies of the predominance of large-scale structures in the outer layer with increasing Reynolds number.

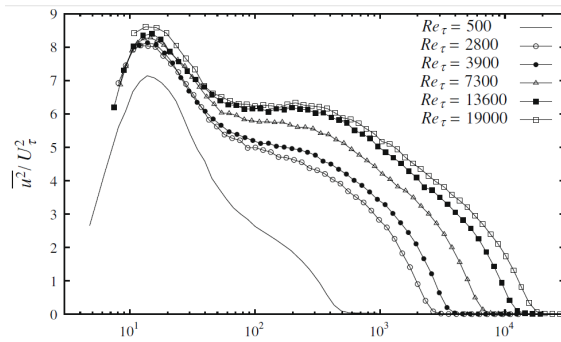


Figure 2.4.: Streamwise turbulence intensity profile at increasing friction Reynolds numbers [15]

The energetic signature of the turbulent superstructures is also to be seen in streamwise premultiplied energy spectra, as represented in figure 2.5. The premultiplied energy spectra advantageously represent the amount of energy pro characteristic wavelength, and their integral is equal to the turbulence intensity profiles. It features that there is a strong overlap region of the wavelengths of small-scale fluctuations and large-scale motions, and that the latter are predominant in the outer layer.

It has been shown that turbulent superstructures strongly affect the properties of the flows, especially they play an important role in modulating the fluctuations of the flow underneath them. First observed by Head [8] and thoroughly documented by Marusic and Hutchins [15], an amplitude modulation is observed as an effect of the large-scale high speed and low speed events on the near-wall fluctuations. The near-wall streamwise velocity and local instantaneous Reynolds stresses $\langle u^2 \rangle$, $\langle v^2 \rangle$, $\langle w^2 \rangle$ and $\langle uv \rangle$ has been observed to be particularly affected by the large-scale motions in the outer layer. This signature of the turbulent superstructures onto the near-wall flow is referred to as "footprinting", and traditionally observed by correlating the large-scale streamwise velocity at a parallel to the wall reference plane with the considered quantity (velocity component, second order fluctuation moment) at planes underneath it.

The FIK identity [12] highlights the dependency of friction coefficient with the Reynolds stresses $\langle u'v' \rangle$:

$$C_f = \frac{12}{Re} + 12 \int_0^h 2 \left(1 - \frac{y}{h}\right) \langle u'v' \rangle dy \quad (2.6)$$

As it has been shown that the Reynolds stresses are strongly affected by the superstructures, the FIK identity manifests that the friction drag of a flow is also highly dependent on the turbulent superstructures properties.

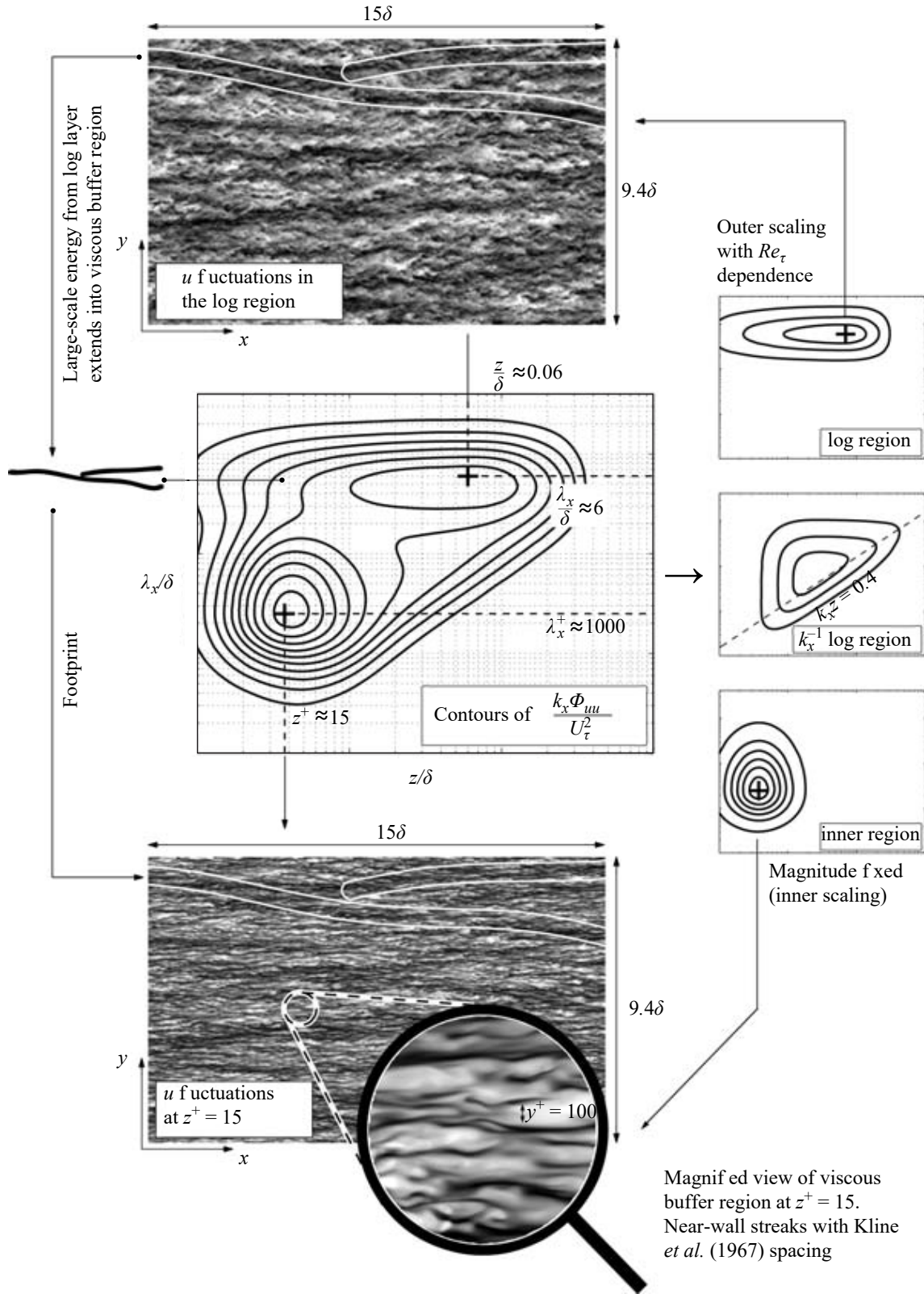


Figure 2.5.: Schematic explaining the relative contributions of small-scale fluctuations and large-scale motions to the premultiplied energy spectra[10]

Extraction of the superstructures from a turbulent flow field

While the existence of turbulent superstructures has extensively been demonstrated via experiments and, since recently, via direct numerical simulations thanks to increasing

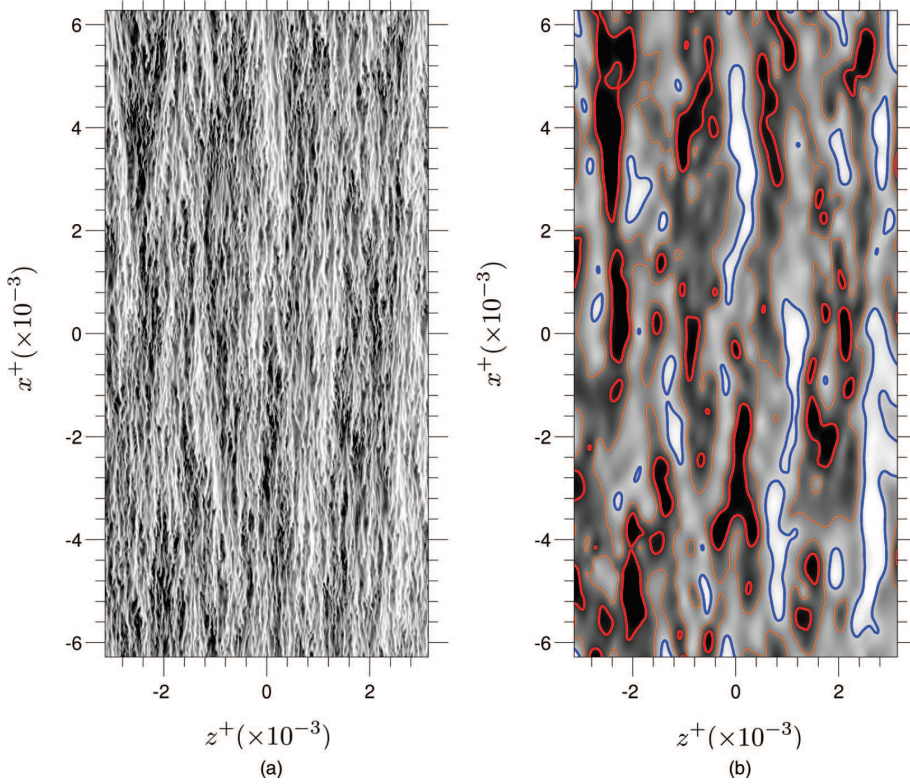


Figure 2.6.: Snapshot of the streamwise-velocity fluctuations at $y^+ = 13.5$: (a) complete signal; (b) large-scale velocity fluctuations; islands with red/blue boundaries identify positive/negative fluctuations within the extreme 10% bands (tails) of the PDF of the large-scale fluctuations [2]

computational resources allowing the simulation of moderate Reynolds number flows, there is no clear-cut definition of these structures.

Studies in which VLSM were extracted from the flow resorted to Gaussian thresholds of the Fourier transforms of the flows. This method relies on the arbitrary determination of the cut-off value, on which the properties of the captured superstructures necessarily depend. However, small-scale and large-scale structures present a strong overlap region, particularly at moderate Reynolds numbers, where there is no real scale separation. The distinction between small-scale turbulence and turbulent superstructures is thus fuzzier than a simple wavelength threshold, as both can contain small and large wavelengths, but at different energy levels.

Recently, an attempt has been made by Agostini and Leschziner [2] to extract superstructures via empirical mode decomposition. This method, presented in 2.3, allows to extract a finite number of modes containing specific bands of increasing lengthscales. Thoroughly arranging these modes in two signals yielded to a small-scale signal, containing the numerous thin and elongated fluctuations of the flow, a large-scale signal, corresponding to the large velocity modulations of the superstructures.

Figure 2.6 presents the velocity fluctuations in a plane parallel to the wall of a turbulent channel flow and its decomposition in small-scale and large-scale signals obtained by Agostini and Leschziner via EMD.

This work aims at implementing a similar bidimensional empirical mode decomposition algorithm, in order to then study the influence of wall-based drag reduction strategies in turbulent channel flows on the turbulent superstructures.

2.2. Drag reduction strategies in wall-bounded turbulent flows

Control strategies of turbulent flows aimed at reducing skin-friction have aroused increasing interest over the past decades. Whether it be in the domains of industry, transports, energy or mechanical sports, improving drag reduction in wall-bounded flows is a challenge of practical importance. At first, the definition of drag reduction is addressed. Then, the classification of the control scheme is presented. At last, one of the most successful drag reduction strategies is presented, the so-called streamwise traveling waves of spanwise wall velocity.

2.2.1. Definition of drag reduction

The use of drag reduction strategies affects the friction coefficient of turbulent wall-bounded flows. The drag reduction achieved by a control strategy is thus defined as the ratio of the friction coefficient of the flow with control over the friction coefficient of the flow without control

$$DR = \frac{C_{f,control} - C_f}{C_f}$$

The friction coefficient of a flow is defined as the wall shear-stress scaled by the kinetic energy of the bulk velocity

$$C_f = \frac{\tau_w}{\frac{1}{2}\rho\bar{U}^2} \quad (2.7)$$

2.2.2. Classification of flow-control strategies

Flow-control strategies can be classified into two main families: the active ones and the passive ones. Active flow-control devices require external energy sources, whereas passive ones work statically. Examples of passive drag reduction strategies can be found in the nature, like the surface of sharks skin. By their dynamical nature, active devices can either be predetermined or react with the environmental flow, with help of feedforward or feedback loops. Reactive drag reduction strategies can adapt the dynamics of the control depending on the real-time flow characteristics thanks to sensors placed in the flow.

The properties of wall-bounded turbulent flows can be accessed either at the wall or away from it. Away from the surface, the flow properties can be modified, for example, via the introduction the so-called large-eddy break-up devices, the generation of acoustic waves propagating through the shear layer, or the generation of magneto- and electrohydrodynamic body forces. At the wall, the properties of the surface (including porosity, geometry, temperature), the suction or injection of fluid or the motion of the wall can be used reduce the skin-friction drag, among other strategies.

For practical reasons, the wall-based drag reduction strategies have found more application and attracted more interest, as they can directly access the vicinity of the wall, where the turbulence generation takes place. The flow control used in the available data of a simulation of a controlled turbulent channel flow is an active predetermined one, using the so-called streamwise traveling waves of spanwise wall velocity, and presented in the following.

2.2.3. Streamwise traveling waves of spanwise wall velocity

Streamwise traveling waves of spanwise wall velocity is a predetermined active flow-control strategy aiming at reducing the skin-friction drag of turbulent flows. Developed by Quadrio *et al.* [18], it is one of the most successful existing drag reduction strategies. Figure 2.7

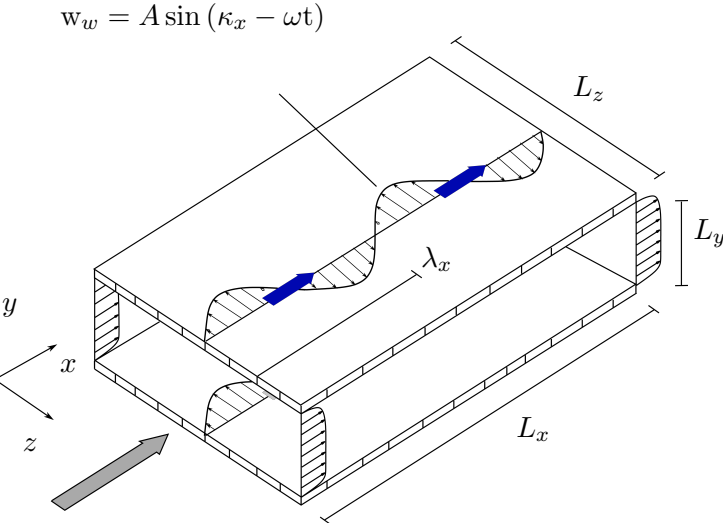


Figure 2.7.: Graphical representation of the streamwise traveling waves of spanwise wall velocity on a turbulent channel flow

present a schematic representation of the streamwise traveling waves of spanwise wall velocity applied to a turbulent channel flow.

The spanwise wall velocity magnitude w_w is sinusoidally modulated in the streamwise direction and can be defined as a function of the streamwise position and the time:

$$w_w = A \sin(\kappa_x - \omega t) \quad (2.8)$$

with $\kappa_x = 2\pi/\lambda_x = 10/h$ the wavenumber in streamwise direction, $\lambda_x = L_x/20 = 0.2\pi h$ the wavelength in streamwise direction and $\omega = 23.8 u_\tau/h$ the frequency of the wave - with the values used to compute the DNS data available in this study. The drag reduction achieved with this method depends on the values of the parameters couple (ω, κ_x) and can reach up to 50% drag reduction. With the values presented here, a drag reduction of 30% can be achieved.

In flows of constant pressure gradient, and thus constant wall shear stress, the implementation of this wall-based drag reduction strategy yields through the drag reduction achieved to an augmentation of the bulk velocity. The mean velocity profiles represented in figure 2.8 illustrate the bulk velocity increase between a flow controlled via streamwise traveling waves of spanwise wall velocity, with wave parameters equal to the values presented above, and an uncontrolled flow computed at the same friction Reynolds number $Re_\tau = 1000$.

2.3. Empirical Mode Decomposition (EMD)

Empirical Mode Decomposition is a data-driven method to decompose nonlinear and non-stationary signals into a finite number of so-called intrinsic mode functions. This method, introduced by Huang *et al.* in 1998 [9], is an adaptive algorithm which provides intrinsic mode functions shapes that arise exclusively from the original data. Thus, unlike Fourier or wavelet decompositions, this method does not rely on predefined base functions. This adaptive feature allows to use empirical mode decomposition on any kind of signal, whether it be linear or not, stationary or not. This places the EMD as an alternative to traditional decompositions, which require such conditions on the signal.

The empirical mode decomposition is a sifting process, in which the intrinsic mode functions (IMF) are iteratively computed. A signal $f(x)$ contains a finite number n of intrinsic

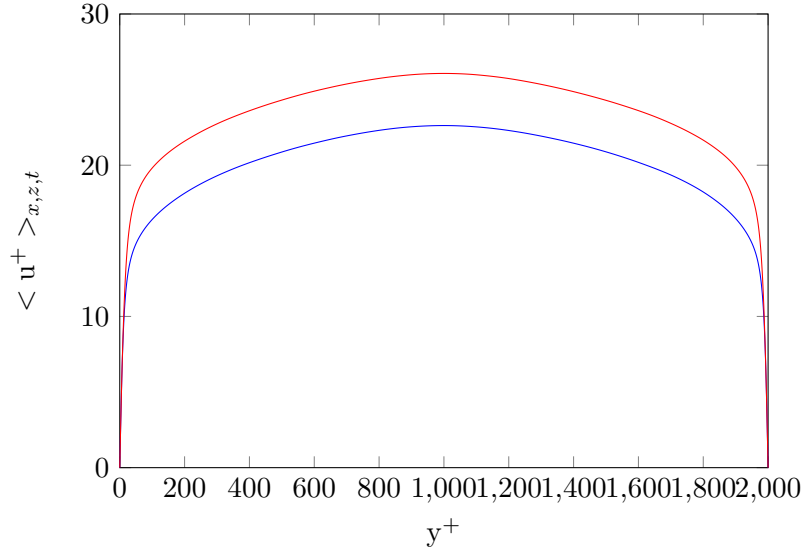


Figure 2.8.: Mean velocity profiles of a controlled (red) and an uncontrolled (blue) channel flow, both computed at $Re_\tau = 1000$

mode functions $IMF(x)$ and a residual $res_n(x)$:

$$f(x) = \sum_{i=1}^n IMF_i(x) + res_n(x) \quad (2.9)$$

After Huang's theory, the intrinsic mode functions have to respect two conditions in order to extract physically meaningful components:

1. have a zero mean envelope
2. have an equal number of zero-crossings and of extrema, or they should only differ by one

In some cases, it might be useful to notice that the second condition is equivalent to having an equal number of maxima and of minima, or they should only differ by one.

Each IMF is obtained via an iterative process, in which the mean envelope of the signal is subtracted from the signal. Figure 2.9 represents a time series of wind speed $v(t)$, its mean envelope $E_{mean}(t)$ and the signal $res(t)$ obtained once $E_{mean}(t)$ has been subtracted from $v(t)$. It is noticeable that through the subtraction, the mean envelope of $res(t)$ has been brought closer to a zero signal. This is still not an IMF as there are some positive local minima or negative local maxima, which betrays a non zero mean envelope of res .

The mean envelope subtraction sifting process is repeated until the conditions on IMF are satisfied. For that, the standard deviation between two consecutive sifting results $res_k(t)$ and $res_{k+1}(t)$ can be introduced as a stopping criterion:

$$SD = \sum_{t=0}^{\tau} \frac{|res_{k+1}(t) - res_k(t)|^2}{res_k^2(t)} \quad (2.10)$$

Once the first intrinsic mode function $IMF_1(t) = v(t) - res(t)$ has been extracted, the signal $v(t)$ is initialized in order to get the next IMF: $v(t) = v(t) - IMF_1(t)$, and so on after each IMF. The decomposition is fully accomplished when the residual contains less than 2 maxima or minima.

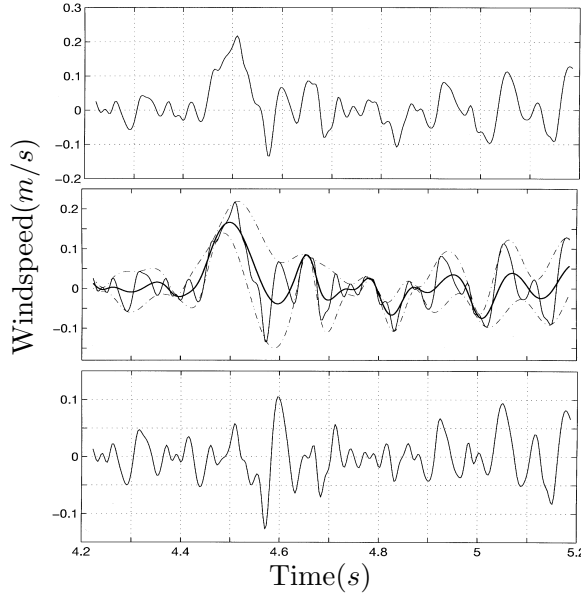


Figure 2.9.: A wind velocity profile $v(t)$, its mean envelope $E_{mean}(t)$ and the residual $res(t) = v(t) - E_{mean}(t)$ [9]

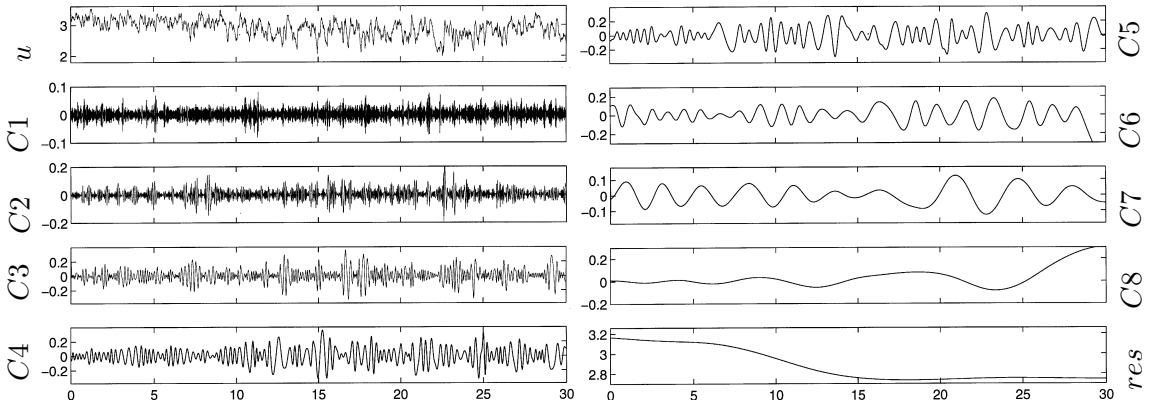


Figure 2.10.: Intrinsic mode functions $C1$ to $C8$ and residual res resulting from the EMD method applied to the wind speed u [9]

The first modes extracted present the highest frequencies and the last ones the lowest frequencies. This is to be seen on figure 2.10, which represents the 8 IMF and the residual obtained via empirical mode decomposition of a wind speed signal.

The mean envelope is computed as the average of the upper and lower envelopes of the signal. The latter are obtained via interpolating the local maxima resp. minima of the signal separately, with the help of cubic spline interpolation functions.

The algorithm to extract n intrinsic mode functions can be expressed as follows:

1. Initialize the residuum: $res = f(x)$
2. a) Extract the local minima and maxima from the residuum res
- b) Interpolate the upper and lower envelopes E_{up} and E_{low} from the local maxima resp. minima
- c) Compute the mean envelope $E_{mean} = (E_{up} + E_{low})/2$
- d) Initialize the residuum:

$$res = res - E_{mean}$$

- e) Subject the residuum to a stopping criterion:
if it is satisfied, the first IMF is obtained $\text{IMF}_1 = \text{res}$
if it is not satisfied, repeat steps 2.a) to 2.e)
3. Initialize the signal f : $f(x) = f(x) - \text{IMF}$
4. Repeat steps 1. to 3. n times

This method can be extended to 2D-signals, in which the envelopes are also computed from the local maxima and minima, but in the two-dimensional space.

3. Empirical mode decomposition for scale separation of 2D-streamwise velocity signals

As mentioned in the introduction, the decomposition of the streamwise velocity of turbulent flows in small scale and large scale motions is computed via empirical mode decomposition (EMD). Previous studies have shown, that the VLSMs meander mainly in the streamwise and spanwise directions of the flow [10]. In order to capture the VLSM meandering nature in the decomposition, it is wished to apply a bi-dimensional extension of the EMD on planes of the flow velocity field at constant wall-normal distances. On this purpose, the first part of this chapter will focus on the description of the available fully developed turbulent flow data, while the second part will focus on the implementation of a low-cost EMD: the so-called fast and adaptive bi-dimensional empirical mode decomposition (FABEMD).

3.1. Preliminary transformations of the flow field

Controlled and uncontrolled fully developed turbulent channel flows are considered in order to study the influence of wall-based control on the large scale motions of the flow. A set of direct numerical simulations of such flows has been provided in the framework of this work. The following part aims first at describing the controlled and uncontrolled available cases, and then at presenting the preliminary computations required before performing the scale separation.

The method used to generate the DNS is aimed for low-cost direct numerical simulation of incompressible turbulent channel flows and was developed by Luchini and Quadrio [14]. The discretization is mixed-spectral, with Fourier modes in the two homogeneous directions and with highly accurate sixth-order compact finite differences in the wall-normal direction:

$$\begin{aligned} u(x, y, z, t) &= \sum_{i_x=-nx}^{n_x} \sum_{i_z=-nz}^{n_z} \hat{u}(i_x, y, i_z, t) e^{j k_x i_x} e^{j k_z i_z} \\ w(x, y, z, t) &= \sum_{i_x=-nx}^{n_x} \sum_{i_z=-nz}^{n_z} \hat{w}(i_x, y, i_z, t) e^{j k_x i_x} e^{j k_z i_z} \end{aligned} \quad (3.1)$$

with $k_x = \frac{2\pi}{L_x}$ and $k_z = \frac{2\pi}{L_z}$ the wavenumbers and i_x and i_z the coordinates in the spectral domain in streamwise and spanwise directions.

Fourier discretization allows simplifying the derivatives of the streamwise and spanwise velocity components in the spectral domain as follows:

$$\begin{aligned} F\left(\frac{\partial u(x)}{\partial x}\right) &= j \hat{u}(i_x) i_x k_x \\ F\left(\frac{\partial w(z)}{\partial z}\right) &= j \hat{w}(i_z) i_z k_z \end{aligned} \quad (3.2)$$

with F the Fourier transform operator and $j^2 = -1$.

The incompressibility constraint is naturally and exactly imposed by projecting the Navier-Stokes equation into a divergence-free manifold, in which the natural variables are substituted by the wall-normal velocity v and wall-normal vorticity $\eta = \frac{\partial u}{\partial z} - \frac{\partial v}{\partial x}$:

$$\begin{aligned} \hat{u}(i_x, i_z) &= \frac{j(\alpha \partial v / \partial y - \beta \eta)}{k^2} \\ \hat{w}(i_x, i_z) &= \frac{j(\beta \partial v / \partial y + \alpha \eta)}{k^2} \end{aligned} \quad (3.3)$$

with $\alpha = i_x k_x$, $\beta = i_z k_z$ and $k^2 = \alpha^2 + \beta^2$. Details of the transformations can be found in the appendix A. The Navier-Stokes equations can then be solved in the wavenumber space, what considerably reduces the computational costs [17].

In order to post-process the streamwise velocity u , it has to be first retrieved from η and $\frac{\partial v}{\partial y}$ - produced by the DNS - after equations 3.3, and then transformed back into the physical space thanks to the inverse Fourier transform.

3.2. Bidimensional scale separation algorithm

Like the one-dimensional EMD, described in 2.3, the bi-dimensional EMD consists in subtracting the mean signal from the raw data to get the next empirical mode decomposition component (EMDC). The mean signal is computed as the average of the upper and lower envelopes of the signal. A conventional way to extract those external envelopes from the local extrema of the signal is to interpolate them, using a bi-dimensional interpolation function. Such an algorithm has been implemented and performed at first, using thin plate spline interpolation [4], which has been determined as a good choice for BEMD [16]. Considering the extreme computational effort and the unsatisfying results, further literature research has been conducted and led to an algorithm adapted to data sets with huge amount of extrema: fast and adaptive bidimensional empirical mode decompostion (FABEMD).

The following section focuses on the description of the FABEMD algorithm and its user-defined parameter w . Then, a quantitative and qualitative comparison between the interpolation-based BEMD and the FABEMD is conducted to highlight the powerful cost reduction and the qualitative improvements brought by the FABEMD.

3.2.1. Fast and adaptive bisimensional empirical mode decomposition

FABEMD is a novel low-cost approach developed by Bhuiyan et Al. [3] for performing two-dimensional empirical mode decompositions. The distinctive feature resides in the order-statistics filter based envelope estimation instead of 2D-scattered data interpolation, which allows to bypass the extreme computational cost of interpolation via a much cheaper algorithm.

Envelope estimation based on order-statistics filters

Order-statistics filters are sliding window filters whose response depends on the ordering of the data covered by the filter. The value taken by the upper envelope of a signal $f(x, y)$ at the point (x, y) is obtained by finding the maximum in the window $W_{x,y}$ of size $[w \times w]$ centered at (x, y) :

$$E_{up}(x, y) = \max_{(i,j) \in W_{x,y}} f(i, j) \quad (3.4)$$

The resulting non-continuous signal is smoothed by computing at each point (x, y) the mean value of the data contained in $W_{x,y}$ to become a continuous envelope:

$$E_{up}(x, y) = \frac{1}{(2w+1)^2} \sum_{(i,j) \in W_{x,y}} E_{up}(i, j) \quad (3.5)$$

In the same way, the lower envelope is estimated by filtering and smoothing the local minima of the signal:

$$\begin{aligned} E_{low}(x, y) &= \min_{(i,j) \in W_{x,y}} f(i, j) \\ E_{low}(x, y) &= \frac{1}{(2w+1)^2} \sum_{(i,j) \in W_{x,y}} E_{low}(i, j) \end{aligned} \quad (3.6)$$

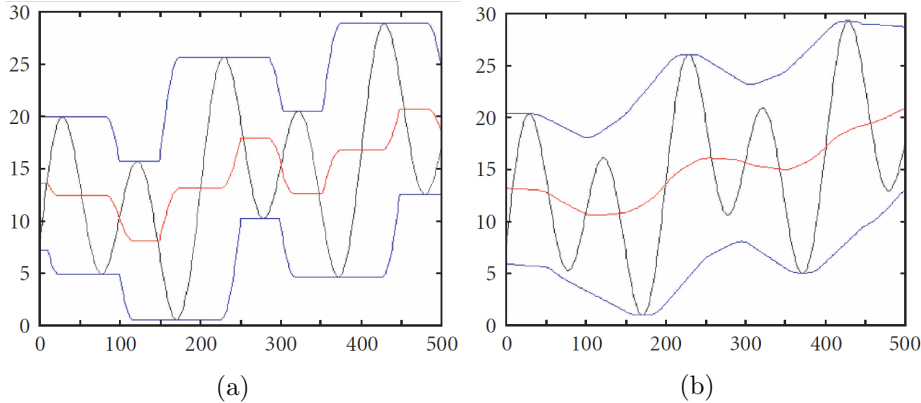


Figure 3.1.: Upper and lower envelopes (blue) using order-statistics filter based estimation, before (a) and after (b) smoothing, and the resulting mean envelope (red) [3]

Figure 3.1 illustrates the upper and lower envelope estimations of a 1D signal. The obtained envelopes are strongly depending on the windowing width, which obviously must increase from mode to mode in order to extract modes of increasing frequencies. According to Bhuiyan's theory, the data-driven window width can be determined from the euclidean distance d between two local maxima respectively minima:

$$\begin{aligned} w_1 &= \min(\min(d_{up}), \min(d_{low})) \\ w_2 &= \max(\min(d_{up}), \min(d_{low})) \\ w_3 &= \min(\max(d_{up}), \max(d_{low})) \\ w_4 &= \max(\max(d_{up}), \max(d_{low})) \end{aligned} \quad (3.7)$$

From the previous definitions of w , results the inequality $w_1 \leq w_2 \leq w_3 \leq w_4$. If the width between two following modes i and $i + 1$ does not increase, which is often the case

with w_1 and w_2 , Bhuiyan added in his paper that the ratio of the two widths should be bigger than a user-defined value - mostly taken equal to 1.5:

$$\text{if } w_{i+1} \leq w_i , \quad \frac{w_{i+1}}{w_i} \geq 1.5 \quad (3.8)$$

It is important to notice here that the narrower the window, the more modes are extracted, and that the computational cost is proportional to the square of the window size.

The local extrema $\max(x, y)$ and $\min(x, y)$ are identified via sliding windows of size $[3 \times 3]$ data points:

$$\begin{aligned} \max(x, y) &= \max_{(i,j) \in W_{x,y}} f(i,j) \\ \min(x, y) &= \min_{(i,j) \in W_{x,y}} f(i,j) \end{aligned} \quad (3.9)$$

Algorithm of the FABEMD

The algorithm of fast and adaptive empirical mode decomposition for extracting n modes can be summarized as follows:

1. Initialize the residuum: $\text{res} = f(x, y)$
2. a) Extract the extrema MIN and MAX of the residuum res
- b) Define the filter window width w
- c) Compute the upper and lower envelopes E_{up} resp. E_{low} using order-statistics filters with the width w
- d) Compute the mean envelope $E_{mean} = (E_{up} + E_{low})/2$
- e) Subtract the mean envelope from the residuum res to get the IMF:

$$\text{IMF} = \text{res} - E_{mean}$$
3. Initialize the residual: $\text{res} = \text{res} - \text{IMF}$
4. Repeat steps 2 and 3 n times

One additional advantage of the FABEMD is that only one iteration is required to extract each EMDC, unlike interpolation based EMD which requires several iterations to converge.

As the implemented FABEMD is meant to be applied to periodic velocity fields, a periodicity condition has been added in the envelope estimation process in order to conserve this periodical nature throughout the decomposition.

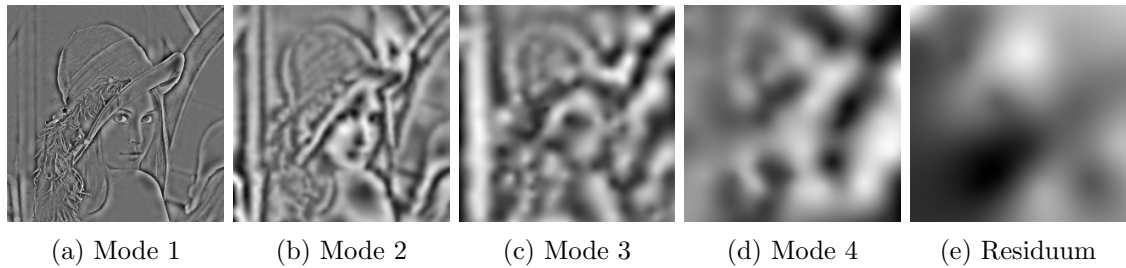
3.2.2. FABEMD vs. BEMD

After having implemented the FABEMD, the quality of its decomposition and the computational costs have been compared with the ones of the BEMD implemented at first, based on a 2D-scattered data interpolation function. The Lena picture, a classical picture in image processing, has been used for this purpose and is represented on figure 3.2.

The interpolation-based bi-dimensional EMD was implemented using the thin-plate spline interpolation method to build the upper and lower envelopes. This conventional method to interpolate 2D-scattered data relies on minimizing the bending energy of a point constrained thin metal plate [4]. As it is an expensive algorithm which requires several iterations to converge, the corresponding function *tpaps* of Matlab was used to optimize the computational costs.



Figure 3.2.: The Lena picture, 256 * 256 pixels

Figure 3.3.: The 4 modes and the residuum of the Lena picture using the thin plate spline interpolation based BEMD with $SD_{max} = 0.2$

The algorithm is the same as the one defined in 2.3, except that all the signals considered are 2D. The stopping criterion chosen was the standard deviation of two consequent sifting results h_{n-1} and h_n :

$$SD = \sum_{(x,y)} \frac{[h_{n-1}(x,y) - h_n(x,y)]^2}{h_{n-1}^2(x,y)} \leq SD_{max} \quad (3.10)$$

and the limit value $SD_{max} = 0.2$ has been chosen, as suggested in literature [REF]. With this value, 4 modes can be extracted, which are represented on figure 3.3 as well as the residuum. The first mode contains the lowest frequencies and the higher the mode, the larger the frequencies - as expected from Huang's theory [9].

The universality of this method can be questioned, and that the way the stopping criterion is computed is not normed, which means the bigger the data, the bigger the value of the stopping criterion. It thus has to be adapted to each data set we want to decompose.

Furthermore, some effects appear in the first modes, which are not present on the original picture: on the woman's shoulder or on the border of her hat, we observe darker spots which are compensated by lighter spots in the next modes. The modes thus extracted show information that does not exist in the original data, hence we cannot validate this method for a further application to the turbulent flow fields.

Hence, the FABEMD was performed on the same picture with each different parameter as defined in 3.7. The decomposition represented on figure 3.4 has been performed with the window-sizing method w_4 , as it is the only one that provides 4 modes - like the interpolation-based BEMD - and the decompositions using other ones can be found in annex B.

One can remark that, unlike results on figure 3.3, the modes obtained via FABEMD do not seem to contain any artifact. This is a huge improvement, which would mean that the

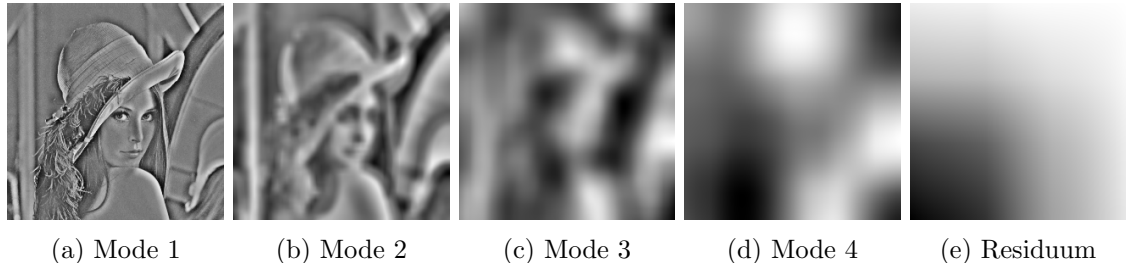


Figure 3.4.: The 4 modes and the residuum of the Lena picture using the FABEMD with the window width w_4

data-driven modes extracted via FABEMD represent the original data split in signals of decreasing frequency domain, without any undesired side effect.

Not only the quality of the decomposition increased by using FABEMD, but also the efficiency of the computation. Table 3.1 resumes the computational time, the mean value, the numbers of maxima and minima and the number of iterations pro mode extracted of the five chosen methods: thin plate spline interpolation based EMD (referred as BEMD) and FABEMD with w_1 , w_2 , w_3 and w_4 .

Table 3.1.: Computational time, mean value, number of maxima and minima, and windowing width for each mode of the decomposition of the Lena picture with the FABEMD method

Method	Mode	Time (s)	Mean	NB min	NB max	w (points)	NB iterations
w_1	1 st	2.07	-0.0019	5725	5791	3	1
	2 nd	1.92	0.0002	1309	1360	5	1
	3 rd	1.89	0.0004	334	346	7	1
	4 th	2.04	0.0004	116	114	11	1
	5 th	2.21	-0.0001	46	48	17	1
	6 th	2.68	-0.0005	22	18	29	1
	7 th	3.60	-0.0021	10	11	47	1
w_2	1 st	2.05	-0.0019	5725	5791	3	1
	2 nd	1.92	0.0002	1309	1360	5	1
	3 rd	1.94	0.0004	334	346	7	1
	4 th	2.06	0.0004	116	114	11	1
	5 th	2.77	0.0003	25	33	31	1
	6 th	8.41	-0.0110	9	6	99	1
w_3	1 st	2.07	-0.0044	3767	3883	9	1
	2 nd	2.79	-0.0021	122	112	31	1
	3 rd	8.65	-0.0132	13	12	101	1
w_4	1 st	2.23	-0.0045	3694	3847	11	1
	2 nd	3.07	-0.0026	79	77	37	1
	3 rd	8.78	-0.0126	12	7	103	1
	4 th	10.30	-0.0031	4	2	115	1
BEMD	1 st	17044.01	0.7560	10353	10980	—	51
	2 nd	73.75	0.7699	159	129	—	23
	3 rd	27.89	0.7788	36	18	—	16
	4 th	14.27	0.8004	3	6	—	11

It is obvious from the table, that the FABEMD presents unbeatable computational costs in comparison with the thin-plate spline based BEMD. The extreme long computational time of BEMD can be put down to the impossibility to parallelize the computation from the essence of the algorithm, and the difficulty for the Matlab function *tpaps* to converge due to a high amount of extrema in the data.

It should be recalled that in Huang's EMD theory, the extracted intrinsic mode functions should fulfill two conditions:

1. have a zero mean
2. have the same number of maxima and minima, or they should differ only by one

The mean of the modes obtained via FABEMD are much closer to zero than the mean obtained via BEMD, and the number of maxima and minima per mode are closer to each other in the FABEMD than in the BEMD. All in all, FABEMD seems to fulfill better the IMF requirements established by Huang than the BEMD.

To sum up, the quality of the decomposition was improved by using the FABEMD method, as outlined in the representations figures 3.3 and 3.4 and in the decomposition statistics of table 3.1, and the computational costs were also strongly reduced (table 3.1). The FABEMD method is consequently the decomposition method used in the following, in order to separate small-scale and large-scale motions in a fully developed turbulent channel flow.

4. Response of VLSM to wall-based friction drag reduction

This chapter aims at presenting the results of scale separation obtained via FABEMD of streamwise velocity in turbulent channel flows. In order to study the influence of wall-based drag reduction strategy on the very large scale motions of the flow (VLSM), controlled and uncontrolled channel flows generated at the same friction Reynolds number are considered, as presented in the previous chapter.

In the first section, the results obtained on an uncontrolled turbulent channel flow with the four different window-sizing methods w_1 , w_2 , w_3 and w_4 (see equation 3.7) of the fast and adaptive empirical mode decomposition (FABEMD) are examined in order to determine which one produces the most physically meaningful scale separation. Then, the small-scale and large-scale signals obtained via this method on the controlled and uncontrolled are presented and compared with each other.

In the last section, a novel approach to compare the VLSM of controlled and uncontrolled turbulent channel flows of constant friction Reynolds number is presented, in which a correlation of the wall skin friction with the large-scale velocity is performed.

4.1. Preliminary study of the FABEMD window-sizing method w

The considered controlled and uncontrolled turbulent channel flows have been computed via the DNS presented in section 3.1. The friction Reynolds number is equal to 1000 in both cases and the channel half height $h = 1$ m. The drag reduction strategy chosen is the streamwise wave of spanwise wall velocity presented in 2.2.3.

As presented in the previous chapter, FABEMD enables to extract modes of increasing typical lengthscales from any kind of bi-dimensional data. The choice of the method w , which defines how the width of the filtering window is computed, plays an important role in the number of modes obtained. The wider the window, the less modes can be extracted and thus the less precise frequencies can be separated - as illustrated with the Lena picture decompositions in appendix B.

Applied to the case of scale separation in turbulent channel flows, the choice of w strongly influences the shape of the VLSM extracted. Hence, it is of major importance to perform a preliminary study on uncontrolled channel flows, in order to determine the most suitable

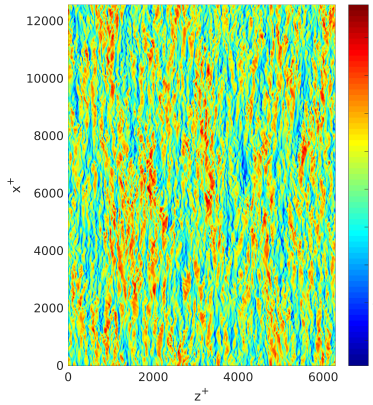


Figure 4.1.: Streamwise velocity component of uncontrolled turbulent channel flow at $\text{Re}_\tau = 1000$ at $y^+ = 13.5$

method and where the delimitation between small-scale and large-scale motions should be set.

The scale decomposition is applied on uncontrolled turbulent channel flows, using as input singular two-dimensional wall-parallel planes of the streamwise velocity component, as represented in figure 4.1. The raw signal is composed of numerous thin streaks, predominantly aligned and very elongated in the streamwise direction, which are advected downstream while evolving in time. Region of much wider extent than the typical size of a streamwise velocity streak can be recognised in figure 4.1, in which velocity fluctuations are predominantly positive or negative, while retaining the finer streaky pattern.

Comparisons of the streamwise turbulence intensity profiles of small-scale and large-scale motions obtained via w_1 and w_2 and obtained via w_3 and w_4 are represented on figures 4.2 resp. 4.3. By definition (equation 3.7), methods w_1 and w_2 provide small windows (hence narrow-window methods from now on), while w_3 and w_4 provide large windows (large-window methods from now on).

4.1.1. The narrow-window methods

For each narrow-window method w_1 and w_2 , the three small-scale signals presented in figure 4.2 have been obtained by adding the first five, six and seven modes. The three corresponding residuals of the signal have been defined as the large-scale signals. Each small-scale and large-scale couple is represented in the same color: red corresponds to small-scale signal containing the first seven, blue six and green five first modes. The profiles obtained with w_1 are plotted with solid lines while the ones obtained with w_2 are represented with cross markers. The highest curves correspond to the small-scale signal, which contain an intensity peak in the inner layer ($y^+ \approx 15$), while the large-scale signals, which contain less turbulence intensity, correspond to the flatter curves.

It appears from this graph that the two methods are superimposed on each other, apart from little fluctuations. This superimposition is actually due to the condition expressed by equation 3.8 in the FABEMD algorithm, which states that the window width should increase between two following modes. This condition is rarely fulfilled with w_1 and w_2 , which provide small window widths. In this case, the window width is artificially set 1.5 times bigger than in the previous mode, which leads to linearly increasing window widths in the two methods.

The two narrow-window methods appear thus to provide similar decompositions. As w_1 fluctuates slightly less than w_2 , it allows to track better the VLSM in the third space

direction, the wall-normal direction. Hence, in the following, w_1 is chosen when referring to narrow-window methods.

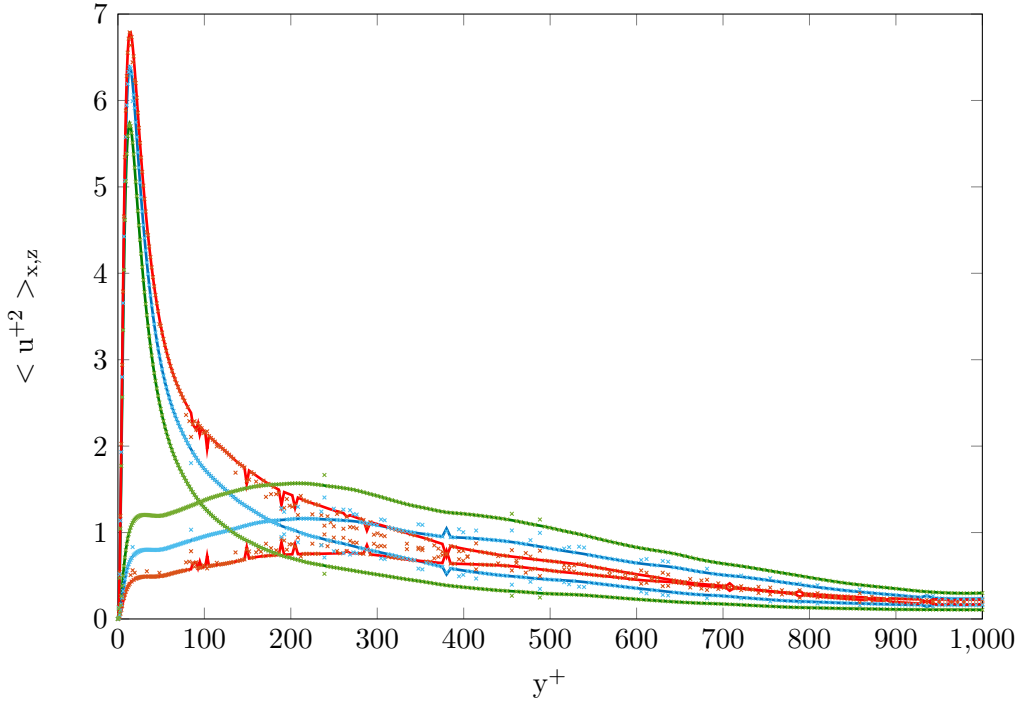


Figure 4.2.: Streamwise turbulence intensity profiles of uncontrolled turbulent channel flow with the FABEMD window-sizing types w_1 (lines) and w_2 (crosses)

4.1.2. The large-window methods

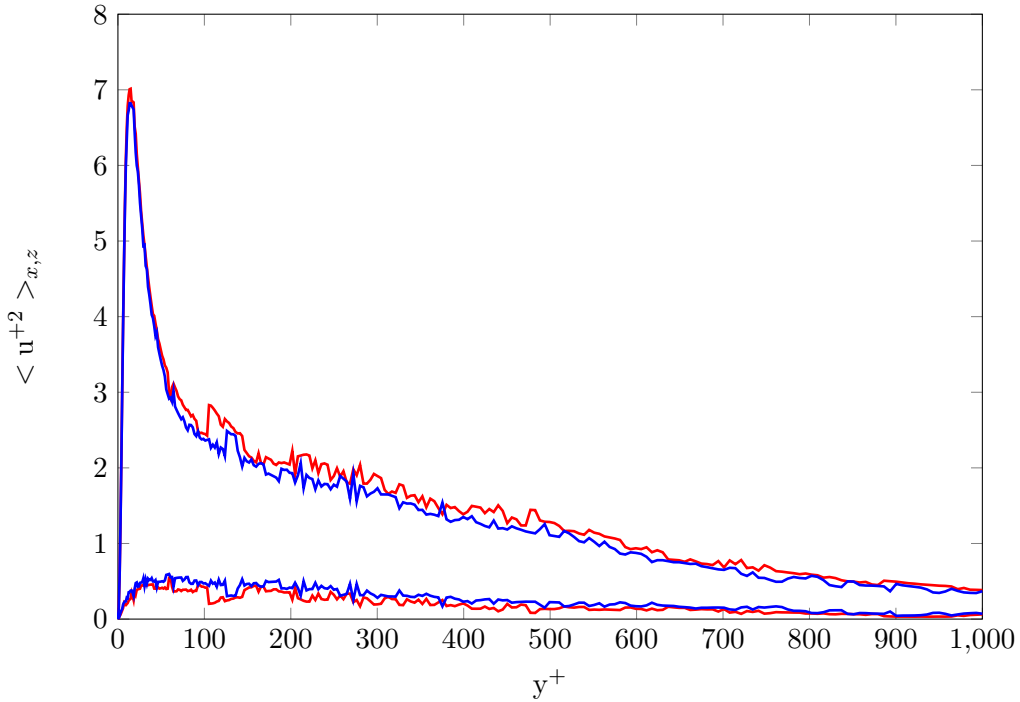


Figure 4.3.: Streamwise turbulence intensity profiles of uncontrolled turbulent channel flow with the FABEMD methods w_3 (blue) and w_4 (red)

For the large-window methods w_3 and w_4 , a similar comparison has been conducted. The small-scale signals have been defined as the sum of the two first modes, and the large-scale signals are the corresponding residuals. The blue curves of figure 4.3 correspond to w_3 and the red ones to w_4 .

Just like with w_1 and w_2 , it appears that both provide similar turbulence intensity profiles, although they fluctuate much more than with the narrow windows. Decomposition with w_4 contains in the outer layer ($y^+ > 50$) slightly more intensity in the small-scale signal than w_3 (and correspondingly less intensity in the large-scale signal). Large-scale motions having been defined as appearing in the outer layer and containing much energy, it suggests that the VLSM could be slightly better extracted from the signal with w_3 . Moreover, the computational costs of w_3 are lower than the ones of w_4 . Hence, from now on, the less expensive and more physically meaningful of two large-window methods is retained: w_3 .

The four possible methods w_1 , w_2 , w_3 and w_4 can thus be reduced to only two, the narrow-window method w_1 and large-window method w_3 , the other two choices yielding essentially equivalent results. Narrow-window methods are more likely to produce more modes than large-window ones, which increases the computational costs and the storage space requirement (see section 3.2.2). It is thus important to know if the scale separation provided via w_3 is satisfying or if it is needed to invest more and perform narrow-window FABEMD.

4.1.3. Narrow-window vs. large-window methods

Figure 4.4 shows the turbulence intensity profiles obtained with those two window-sizing methods. Similarly to the plots from figure 4.2, the three large-scale/small-scale couples obtained with w_1 (lines) have been obtained, separately, as the sum of the first n modes and the sum of the following modes plus the residual. The three values of n presented are: 5 (green), 6 (blue) and 7 (red). The small-scale and large-scale profiles obtained with w_3 (red dots) are respectively the sum of the two first modes and the remaining residual.

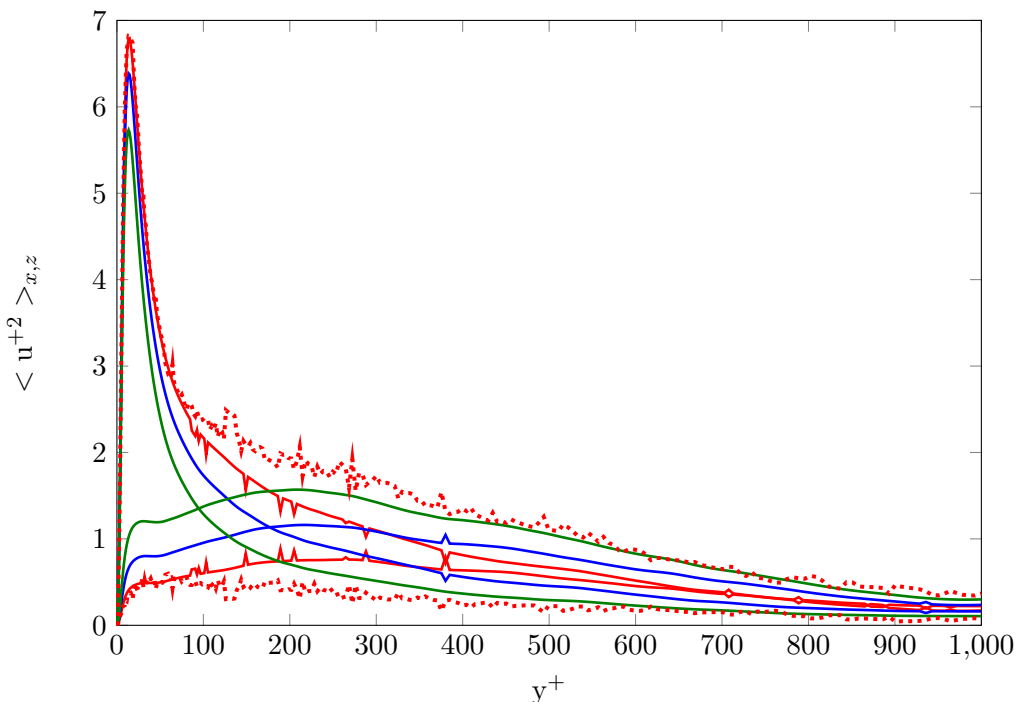


Figure 4.4.: Streamwise turbulence intensity profiles of uncontrolled turbulent channel flow with the FABEMD parameters w_1 (lines) and w_3 (dots)

It appears that the turbulence intensity profiles of VLSM obtained with w_1 present a second peak in the outer layer, at $y^+ \approx 250$, while the one obtained with w_3 does not. They also present the same shape, but seem to be shifted in amplitude: the more modes n are contained in the small-scale signal, the higher the turbulence intensity at any point of this signal (and subsequently the smaller the intensity at any point of the large-scale signal). This suggests that the behavior of the VLSM obtained via narrow-window filtering with 5 to 7 modes in the small-scale signal along the wall-normal direction would be qualitatively similar, but shifted in intensity. To compare further the decompositions obtained via narrow-window and large-window filtering, $n = 7$ is chosen in the narrow-window method, as it features so much turbulence intensity at the inner peak as the large-window method does.

In order to discuss the physical meaning of those two decompositions, the streamwise pre-multiplied energy spectra $k_x \Phi_{uu}^+$ are observed, as represented in figure 4.5. They represent the amount of energy pro streamwise wavelength λ_x across the wall-normal distance y^+ . Thus, it is possible to evaluate if the small-scale and large-scale motions extracted actually contain energy at small and large wavelengths respectively. A prerequisite to physically meaningful power spectral densities is the periodicity of the input signal in streamwise and spanwise directions, as it is computed by applying the Fourier transform operator in these two directions. This constraint is imposed in the raw signal by the DNS and preserved by the decomposition.

Both large-scale signals do not contain any energy at small wavelengths but the small-scale signals features some long wavelengths components. As shown in figure 4.1, those motions are actually thin and long streaks moving in the streamwise direction, which can feature lengthscales fast up to the computational box length - for the longest. It is thus also physically meaningful to extract a part of large wavelengths in the small-scale signal.

The two methods provide small-scale signals of similar energy repartition in the inner region, which is consistent with the turbulence intensity profiles in figure 4.4 (which represent the integral of $k_x \Phi_{uu}^+$ in the x-direction). They feature well the predominance of the small-scale fluctuations in the near-wall region.

In the outer region, the repartition of the energy between small-scale and large-scale signals depends on the window-sizing type. With w_3 , the large-scale signal presents a peak of energy at $y^+ \approx 55$, while with w_1 , it is located further from the wall at $y^+ = 230$ and of higher amplitude (0.07 vs. 0.05), the difference of energy being compensated by more energy in the small-scale signal of w_3 than in the one of w_1 . The peak at $y^+ = 230$ corresponds to the outer peak observed in the $\langle u^+ u^+ \rangle$ profiles in figure 4.4. This distribution of the energy in the small-scale and large-scale motions with w_1 corresponds to Agostini and Leschziner's preliminary analysis of turbulent channel flows at $Re_\tau = 1025$, from which it is expected to obtain a small-scale energy spectrum centered at the inner peak and a large-scale one centered at the outer peak. Thus, method w_1 seems more able to catch the large wavelength fluctuations in the large-scale signal than w_3 , with which the small-scale signal is contaminated by large-scale fluctuations in the outer layer.

It might be noticed that the maximal large-scale energy levels are contained in wavelengths of the computational box length order. This corresponds to infinitely long meandering motions - as the flow is periodic in the streamwise direction. This characteristic however does not appear through the premultiplied energy spectra presented by Leschziner and Agostini [2], where the contour of the VLSM peak appears to be closed. This difference could be explained by a non periodicity of the modes extracted via Agostini and Leschziner's empirical mode decomposition, which would mathematically lead to the existence of energy levels at larger wavelengths, while the modes extracted via FABEMD have been seen to be periodic.

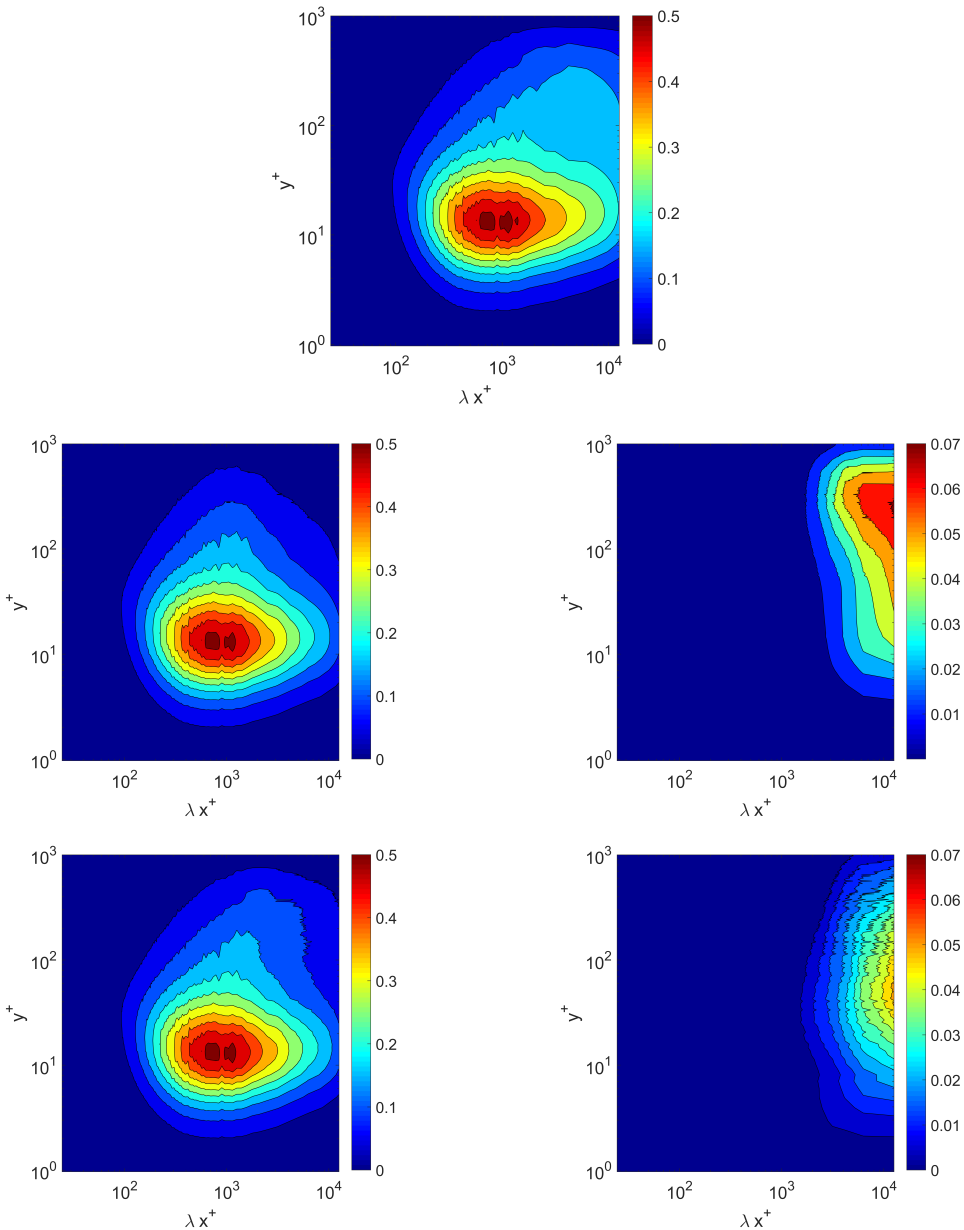


Figure 4.5.: Premultiplied energy spectra of an uncontrolled turbulent channel flow of the streamwise velocity (top), its small-scale signal (center) and large-scale signal (bottom) obtained with w_1 (left) and w_3 (right)

From the analysis of the $\langle u^+ u^+ \rangle$ fluctuations and the premultiplied energy spectra obtained via the different window-sizing methods w , w_1 with $n = 7$ modes seems to be most adapted method to deliver physically meaningful scale separation of the streamwise velocity in turbulent channel flows, in which the small-scale signal corresponds to the sum of the seven modes and the VLSM the residual.

4.1.4. Results

Figure 4.6 shows the results of the decomposition with this method of the streamwise velocity represented in figure 4.1 in large-scale and small-scale motions. The small-scale motions obtained via this decomposition feature well the profuse elongated streaks observed in the raw signal, without its large amplitude modulations, while these modulated regions are seen to match the high and low velocity events of the very alrge scale motions

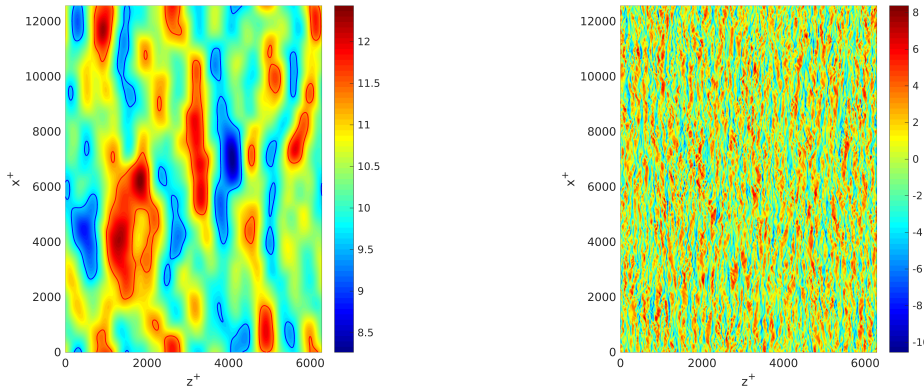


Figure 4.6.: Large-scale (left) and small-scale (right) fluctuations of the streamwise velocity represented in figure 4.1 obtained via w_1 with $n = 7$

extracted. These figures also highlight the conservation of the streamwise and spanwise periodic nature of the raw velocity field through the scale separation.

To sum up, the preliminary study, performed on uncontrolled channel flows, shows that the narrow-window filtering method w_1 seems to be the most adapted to perform a scale separation of fully developed turbulent channel flows. It respects the periodicity of the input signal, the obtained very large scale motions feature a peak in turbulence intensity in the outer region and contain energy only in large wavelengths, and the obtained small-scale motions predominate in the inner layer.

4.2. Scale decomposition of controlled and uncontrolled flows

The scale decomposition has been applied to controlled and uncontrolled turbulent channel flows as described in 2.2.3 and 2.1.1 respectively, which were computed with the direct numerical simulation method presented in 3.1. Both DNS have been performed at the friction Reynolds number $Re_\tau = 1000$, in order to observe how the drag-reduction strategy influences the dynamics of the flow at constant pressure gradient, and particularly if it affects the very large scale motions.

4.2.1. Turbulent superstructures captured

Figure 4.7 represents the large-scale signals obtained in drag-reduced and unmodified flows at a normal distance to the wall $y^+ = 13.5$. It shows that the VLSM of controlled flows present a more organized structure. They appear more elongated and feature a more defined pattern of alternative high-velocity and low-velocity events in the spanwise direction.

4.2.2. Premultiplied energy spectra

The premultiplied energy spectra of controlled and uncontrolled channel flows, each one computed from 16 fields, are represented on figure 4.8. The controlled flow features a lower energy level at the inner peak (0.44 vs. 0.51), which is still located in the inner layer ($y^+ \approx 14$) but has been shifted to smaller wavelengths (≈ 500 vs. ≈ 700). The small-scale and large-scale spectra also present lower peaks of energy and slightly different forms - according to the modifications of the streamwise velocity spectrum. However, the amount of energy contained in the large-scale signal proportional to the energy of the total signal seems higher in the controlled case. It is evident from figure 4.8 that the energy distribution has been modified by the introduction of wall-based drag reduction control, but it does not provide preciser information.

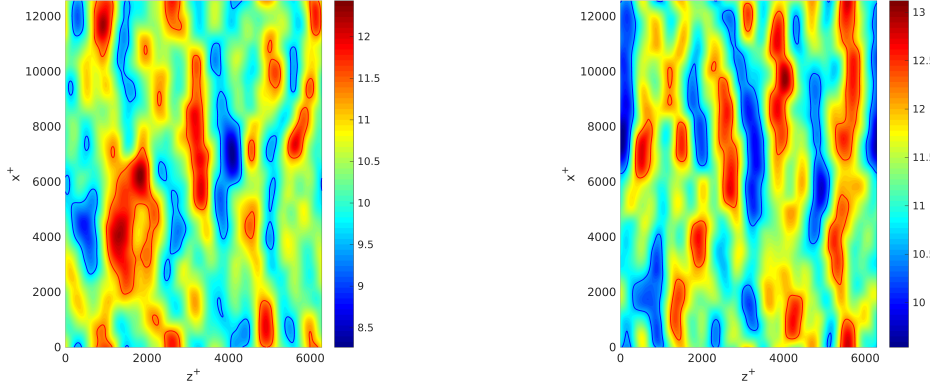


Figure 4.7.: Large-scale fluctuations of the streamwise velocity of an uncontrolled (left) and a controlled (right) flow represented in figure 4.1 obtained via w_1 with $n = 7$

4.2.3. Cross-correlations of the fluctuations across the flow height

In order to highlight the modifications of the small-scale and large-scale motions caused by the streamwise wave of spanwise wall velocity, some cross-correlations in the streamwise and wall-normal directions have been performed.

Small-scale fluctuations

Similarly to the study presented by Agostini and Leschziner [2], the normalized cross-correlation

$$R_{SS}(\Delta x^+, y^+) = \frac{\langle u_{SS}(x^+ + \Delta x^+, y^+) u_{SS}(x^+, y^+ = 13.5) \rangle}{\sigma_{y^+} \sigma_{y^+ = 13.5}}$$

of the small-scale signals of the whole field with the one at the wall-normal distance $y^+ = 13.5$ has been computed, with σ_{y^+} the variance of u_{SS} at y^+ . The plane $y^+ = 13.5$ corresponds to a reference plane in the inner layer, region predominated by the small-scale motions.

As shown in figure 4.9, the correlation of the small-scale of the reference plane with the planes located above it does not experience major modifications with the use of the wall-based drag reduction control, but the correlation towards the wall decreases faster than in the uncontrolled case ($y^+ < 13.5$). It confirms that the control accesses the near-wall quasi streamwise vortices in order to achieve drag reduction.

Large-scale fluctuations

Similarly, the cross-correlation

$$R_{LS}(\Delta x^+, y^+) = \frac{\langle u_{LS}(x^+ + \Delta x^+, y^+) u_{LS}(x^+, y^+ = 150) \rangle}{\sigma_{y^+} \sigma_{y^+ = 150}}$$

of the VLSM with a reference plane located in the outer layer, taken at $y^+ = 150$, is represented in figure 4.10. It appears that, in the controlled case, the VLSM de-correlate faster towards the wall than they do in the uncontrolled case, and their correlation is not so much extended in the streamwise direction.

Two hypothesis can be considered to explain the origins of those differences. Either they result from a structural modification of the flow dynamics caused by the wall-based drag-reduction control, or they are apparent modifications due to an arbitrary choice of scaling.

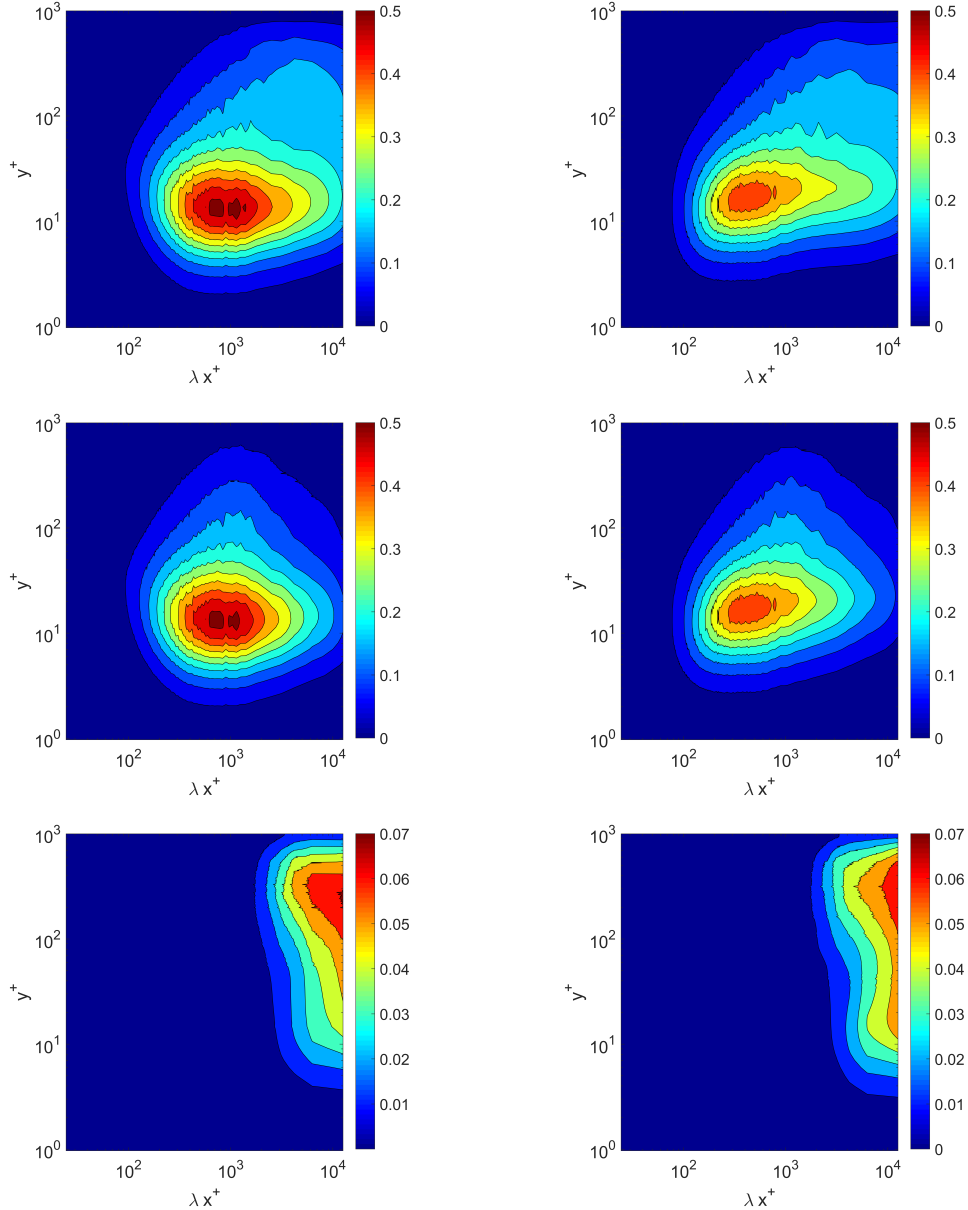


Figure 4.8.: Streamwise premultiplied energy spectra with whole velocity signal (top), the small-scale motions (center) or the large-scale motions (bottom) of uncontrolled (left) and controlled (right) turbulent channel flows

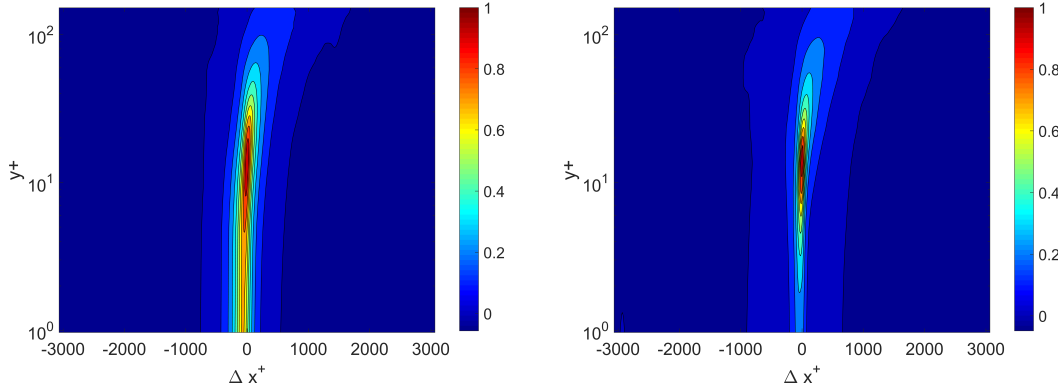


Figure 4.9.: Cross-correlation R_{SS} of the small-scale velocity u_{SS} with the inner layer, in the uncontrolled (left) and the controlled (right) channel flow fields, obtained from 5 snapshots of each flow

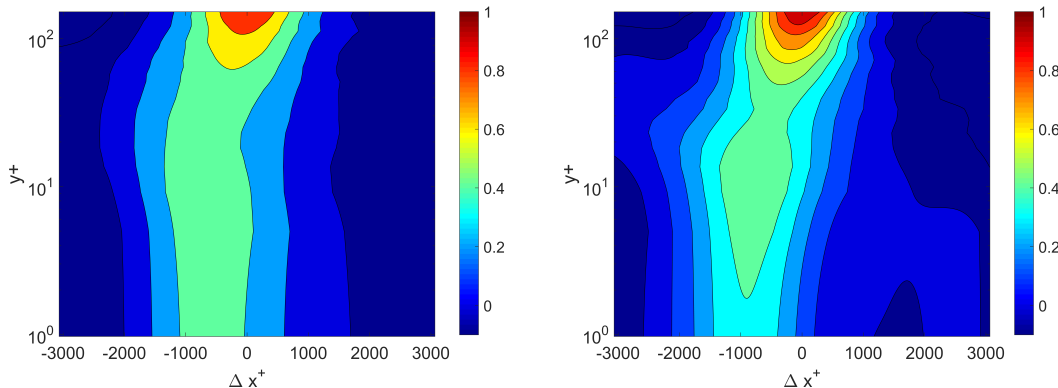


Figure 4.10.: Cross-correlation R_{LS} of the large-scale velocity u_{LS} with the outer layer, in the uncontrolled (left) and the controlled (right) channel flow fields, computed on 5 snapshots of each field

The controlled and uncontrolled flow fields having actually been computed at the same friction Reynolds number $Re_\tau = 1000$, the bulk velocity is higher than without control (figure 2.8). The repeated VLSM in the outer layer seep faster and are thus more often renewed, which - considering Taylor's frozen field hypothesis - could correspond to a lower correlation of the outer region with the near-wall layer. If the flows were computed at constant bulk Reynolds number, the arbitrary chosen reference planes might have another meaning, as the bulk velocity would have stayed constant but the wall shear stress would have decreased.

It seems from figures 4.8 and 4.10 that the use of the streamwise traveling waves of spanwise wall velocity modified the energy distribution in the flow and particularly the large-scale structures of the flow. Aiming at determining if those changes in the correlation are structural or apparent, correlations with other reference planes have been carried out and are presented in the next section.

4.3. Correlation of the friction velocity with the VLSM fluctuations

The correlations performed with a reference plane located in the logarithmic layer have shown to be misleading, as the drag-reduced turbulent flow does not scale like the un-

controlled one. In order to bypass this issue and get comparable data of the controlled and uncontrolled cases, it has been chosen to perform a cross-correlation of the flow with a reference plane at the wall. The two simulations, run at the same friction Reynolds number $\text{Re}_\tau = 1000$, should feature the same dynamics close to the wall, where wall units scaling is still valid.

As the VLSM are also known to correlate well with the large-scale fluctuations of the skin-friction signal - the so-called foot-printing of the superstructures [1] - it has been chosen to perform the correlation of the large-scale motions with the friction velocity

$$R(\Delta x^+, y^+) = \frac{\langle u_{LS}(x^+ + \Delta x^+, y^+) u_\tau(x^+, y^+ = 0) \rangle}{\sigma_{u_{LS}} \sigma_{u_\tau}}$$

Such correlations are represented in figures 4.11 for respectively uncontrolled and controlled channel flows.

The trend of both correlations is similar, featuring a correlation decreasing away from the wall, and which center is shifted backwards the stream direction up to $y^+ \approx 50$ and forwards further to the wall. The maximum also features the same value at the wall, which confirms, as the same statistical wall friction velocity $\langle u_\tau \rangle = 1 \text{ m/s}$ is imposed by the DNS, that the two flows feature the same dynamics close to the wall. However, the correlation extend appears to be shrunk in the controlled case at a distance to the wall $y^+ \approx 30$, the contours seem more bent and the correlation decreases faster towards the wall than in the uncontrolled case.

In order to highlight those differences, figure 4.12 represents the difference percentage between the two previous correlations. It shows that at the wall, the controlled flow correlates more than the uncontrolled one in the backwards direction (6%) but less in the streamwise direction (18%). As the wall moves sinusoidally in the spanwise direction, the flow close to the wall follows the wall displacement. The correlation in a plane (x, y) is thus lost where the near-wall fluctuations have moved in the spanwise direction. It translates into the shrinkage observed in figure 4.11 and the lower correlation of controlled flows at positive streamwise displacements close to the wall observed in figure 4.12.

Figure 4.12 shows also that, in the outer layer and for positive streamwise displacements, the large fluctuations of the controlled flow correlate 6% more with the friction velocity than in the uncontrolled flow. It suggests that, despite a faster loss of the correlation in the near-wall layer, the foot-printing of the turbulent superstructures above the large-scale fluctuations of the friction velocity has actually been heightened by the drag reduction strategy. Moreover, the slope of the contours down to the wall appears to be bigger and show a slight curve in the controlled case.

Figure 4.13 represents similar correlations $R(\Delta z^+, y^+)$, performed in the spanwise direction. It appears that, while the correlation of uncontrolled channel flows is perfectly centered at $\Delta z^+ = 0$ and symmetric - as expected -, the controlled flows feature a correlation which is shifted towards positive spanwise displacement Δz^+ at $y^+ \approx 40$. The flow being imposed periodic in the spanwise direction by the DNS and the wall moving sinusoidally in the spanwise direction, the observed correlation is expected to be statistically symmetric. It should be recalled that the presented correlations have been performed on only 16 flow fields, which is little, especially in the spanwise direction, where only a few large-scale structures are present in computational box width. Further investigation on more flow fields should be performed to confirm the symmetry of the spanwise correlation.

To sum up, correlations of the large-scale velocity fluctuations with the skin-friction signal have been performed, allowing the comparison of the dynamics of controlled and uncontrolled turbulent flows. This has been enabled by computing the statistical correlations

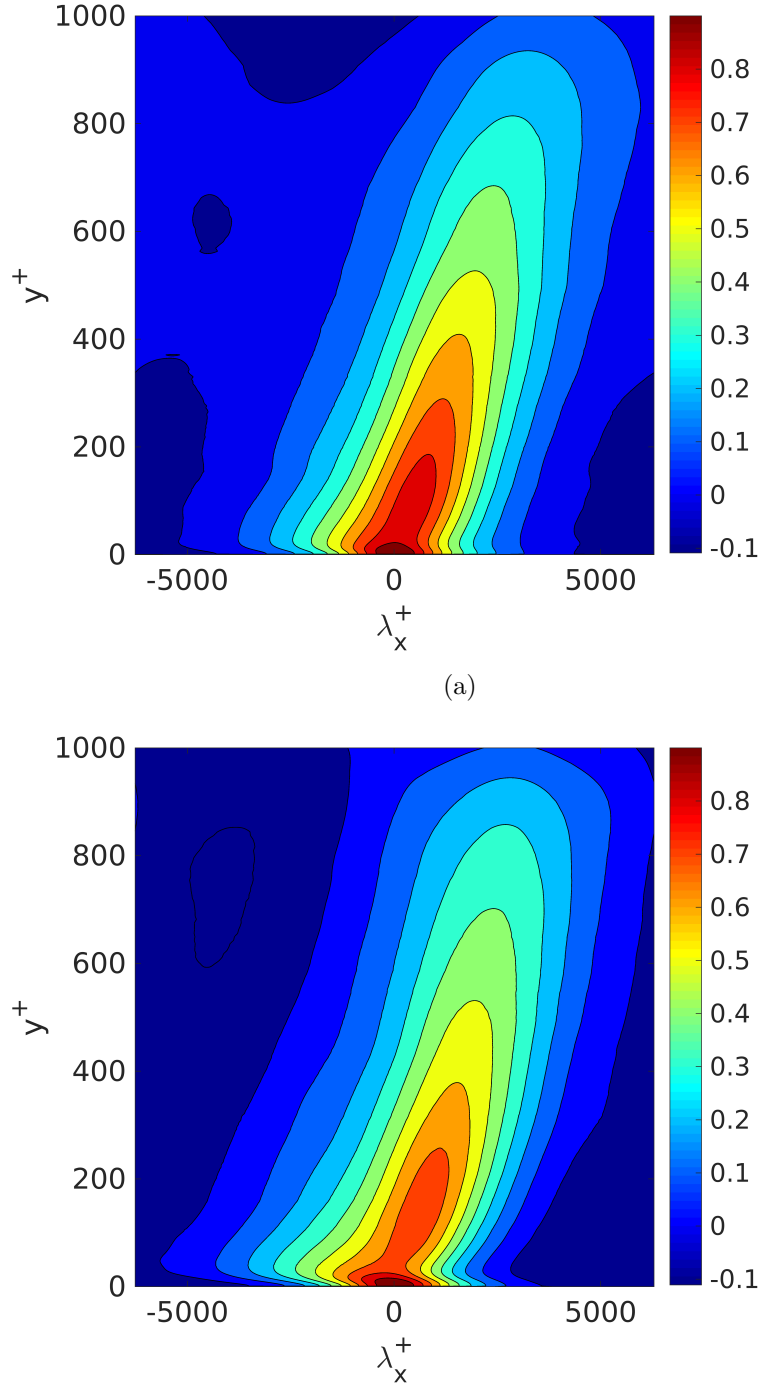


Figure 4.11.: Streamwise cross-correlation of the large-scales wall friction velocity with the VLSM velocity in the controlled (a) and uncontrolled (b) case, averaged on 16 snapshots of the flow field

$R(\Delta x^+, y^+)$ and $R(\Delta z^+, y^+)$ of the large-scale streamwise fluctuations with the friction velocity. It showed that the spanwise moving nature of the studied wall control strategy leads to a reduced correlation extend in the streamwise direction at $y^+ \approx 40$. This correlation could also exhibit an intensification of the foot-printing on the shear stresses. In the meanwhile, the large-scale structures of the outer layer appear to correlate more with the wall friction signal in presence of drag reduction. The spanwise correlation showed an asymmetry in the controlled case, which should find origins in the lack of fields to perform statistical correlations in this direction.

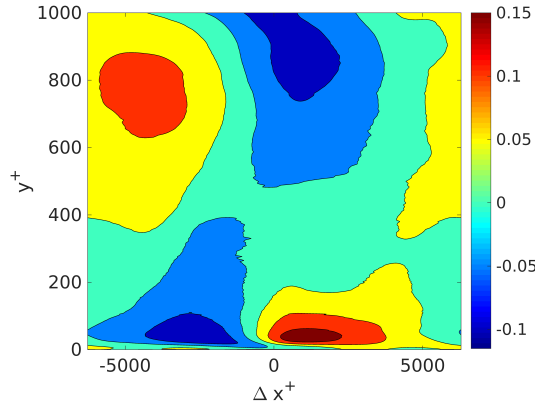


Figure 4.12.: Relative difference $\frac{R_{uncontrolled}(\Delta x^+, y^+) - R_{controlled}(\Delta x^+, y^+)}{\max(R_{uncontrolled}(\Delta x^+, y^+))}$ between the correlations of controlled and uncontrolled flow fields

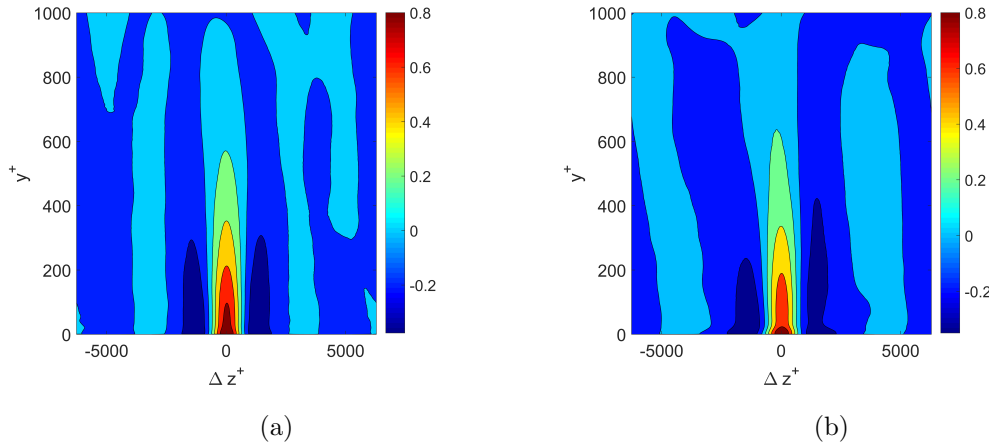


Figure 4.13.: Spanwise cross-correlation of the large-scale wall friction velocity with the VLSM velocity in the controlled (a) and uncontrolled (b) case, averaged on 16 snapshots of the flow field

4.4. Concluding discussion

In this chapter, we addressed a preliminary analysis of the four window-sizing methods of the FABEMD on a turbulent channel flow. The study of the turbulence intensity of small-scale and large-scale fluctuations revealed that they can be reduced to the narrow-window parameter w_1 and the large-window parameter w_3 , as the other apparently provide similar results. Examination of $\langle uu \rangle$ fluctuations and premultiplied energy spectra revealed that the small-scale modes obtained via w_3 are contaminated by large-scale motions, which lead to w_1 being the most suited method for scale decomposition of fully developed turbulent channel flows. The decomposition still features an arbitrary choice of the number of modes regrouped to constitute the small-scale signal, which has been set to 7.

Comparison of large-scale structures obtained on controlled and uncontrolled flows highlighted a higher organization of the turbulent superstructures in the spanwise direction, and high and low velocity events that are more extended in the streamwise direction. Decreasing streamwise correlations towards the wall of a the small-scale fluctuations in a reference plane parallel to the wall and planes above and underneath it showed that wall-based drag-reduction control hinders the near-wall turbulence generation. Similar correlations of the large-scale fluctuations with a reference plane in the outer layer fea-

tured a lower streamwise extend and a faster decorrelation towards the wall in controlled cases. The question of the origin of these differences raises the issue of determining comparable reference planes in the outer layer of controlled and uncontrolled flows of constant wall shear-stress. It has been bypassed by performing the streamwise correlation of small-scale fluctuations in planes parallel to the wall with the friction velocity. It pointed up an increase of the foot-printing effect of the turbulent superstructures on the large-scale skin friction components, while the correlation is lost near to the wall. The apparent pattern exhibited deserves however further investigation to highlight the origins of the superstructures response to wall-based drag reduction.

5. Conclusion

Effects of wall-based turbulent drag reduction on the statistical properties of different scales in turbulent flows, and particularly the so-called turbulent superstructures, have been investigated by comparing drag-reduced and unmanipulated turbulent channel flows.

As the methodology is concerned, a new efficient parallel distributed memory algorithm for the postprocessing of turbulent flow data has been developed in Matlab, which allows to extract data-driven modes of increasing characteristic length scales: the bidimensional empirical mode decomposition. This 2D extension of Huang's empirical mode decomposition is based on the thin plate spline interpolation, an interpolation of 2D-scattered data based on radial basis functions.

Considering the immense computational costs and the unsatisfying results, containing artifacts, further variants of the empirical mode decomposition proposed in the literature have been considered and tested. The tradeoff between performance and complexity yields to the fast and adaptive empirical bidimensional mode decomposition, which relies on order-statistics filters based envelope estimation instead of interpolation. This distinctive feature allows to improve the quality of the modes extracted and reduce considerably the computational costs. Validation of the implemented algorithm has been conducted via comparison to the literature, applied to image-processing standard pictures.

Based on this method, several algorithms to capture superstructures, i.e. large-scale velocity fluctuations in turbulent flow fields, have been successfully implemented in Matlab. The spectral data η and $\partial v / \partial y$ delivered by direct numerical simulations have been transformed to get the velocity components u , v and w in the real domain. Those methods differ in the filtering windows size determination used in the FABEMD algorithm, which strongly influences the number of modes extracted. A preliminary analysis of the decompositions obtained with these methods, performed on uncontrolled canonical flows, addressed that the 4 methods can be reduced to a narrow-window and a large-window one, the two others delivering similar results. The examination of turbulence intensity profiles and premultiplied energy spectra determined that the narrow-window method is the most suitable to extract large-scale motions that feature the statistical properties of turbulent superstructures, delivering thereby a systematic way to perform scales separation.

Turbulent channel flows, in which the drag has been actively reduced by streamwise traveling waves of spanwise wall velocity, have been investigated via this method and compared to unmanipulated canonical flows, performed at the same friction Reynolds number $Re_\tau = 1000$. The extracted turbulent superstructures feature a more organized structure,

which presents a longer extend in streamwise direction and a more defined pattern of alternatively high and low velocity events in the spanwise direction.

The alteration of the turbulence generation process by the skin-friction strategy has also been outlined by a quicker decrease of the statistical correlation of the small-scale fluctuations at a reference plane in the near-wall layer with the planes above and underneath.

However the traditional way of addressing the footprinting effect, i.e. by correlating the streamwise velocity fluctuations at a reference plane located in the log-layer with planes underneath, is found to be misleading and not well defined when comparing unmanipulated flows with drag-reduced ones. In fact, the flows scale differently and thus a reference plane is not guaranteed to have the same meaning in controlled and uncontrolled case.

A novel way of observing the footprinting has been addressed by computing the correlation of the friction velocity and the large-scale fluctuations in wall-parallel planes. It exhibited an increase of the correlation of turbulent superstructures on skin-friction signals, as well as a zone of lower correlation in the near-wall region due to the moving nature of the control used.

Further investigation deserves to be conducted to inspect the causes of the near-wall differences observed in the correlations and the origins of the higher foot-printing. In order to complete the investigation of the effects of wall-based drag reduction on the flow dynamics in the outer region, it could be interesting to conduct similar systematic scale decomposition and footprinting observation on controlled and uncontrolled flows computed at constant bulk velocity. More generally, this powerful systematic scale decomposition opens the door of more in-depth and systematic analysis of the superstructures. This finds many practical applications, as understanding the dynamics of such structures plays a key role in the design of the flow-control strategies of the future.

Symbols and Abbreviations

Roman

C_f	friction coefficient
d	euclidean distance
DR	drag reduction
E	signal envelope
F	Fourier transform operator
h	channel semi-height
j	unit imaginary number
k_x	streamwise wavenumber
L_x, L_y, L_z	dimensions of the computational box
MIN, MAX	ensemble of the local minima resp. maxima of a signal
p	pressure
Re	bulk Reynolds number
Re_τ	friction Reynolds number
res	redisual
SD	standard deviation
u	streamwise velocity
u_τ	friction velocity
v	wall-normal velocity
w	spanwise velocity
w_w	spanwise wall velocity
w_1, w_2, w_3, w_4	window-sizing method of the FABEMD
$W_{x,y}$	window centered at the point (x, y)

Greek

η	wall-normal vorticity
ν	kinematic viscosity
ρ	density of the fluid
τ_w	wall shear stress
σ	variance
δ_ν	viscous length
λ_x	streamwise wavelength

Superscripts

$+$	quantity scaled with the viscous scales
\hat{u}	spectral velocity corresponding to u

Abbreviations

BEMD	bidimensional empirical mode decomposition
DNS	direct numerical simulation
EMD	empirical mode decomposition
FABEMD	fast and adaptive bidimensional empirical mode decomposition
IMF	intrinsic mode function
VLSM	very large scale motions

List of Figures

1.1.	Appearance of turbulent superstructures in a channel flow with increasing Reynolds number	3
2.1.	Channel flow geometry	5
2.2.	The various wall-regions of turbulent channel flows in function of y^+ at high Reynolds number $Re_\tau = 10^4$ [17]	6
2.3.	Appearance of turbulent superstructures in a channel flow with increasing Reynolds number	6
2.4.	Streamwise turbulence intensity profile at increasing friction Reynolds numbers [15]	7
2.5.	Schematic explaining the relative contributions of small-scale fluctuations and large-scale motions to the premultiplied energy spectra[10]	8
2.6.	Snapshot of the streamwise-velocity fluctuations at $y^+ = 13.5$: (a) complete signal; (b) large-scale velocity fluctuations; islands with red/blue boundaries identify positive/negative fluctuations within the extreme 10% bands (tails) of the PDF of the large-scale fluctuations [2]	9
2.7.	Graphical representation of the streamwise traveling waves of spanwise wall velocity on a turbulent channel flow	11
2.8.	Mean velocity profiles of a controlled (red) and an uncontrolled (blue) channel flow, both computed at $Re_\tau = 1000$	12
2.9.	A wind velocity profile $v(t)$, its mean envelope $E_{mean}(t)$ and the residual $res(t) = v(t) - E_{mean}(t)$ [9]	13
2.10.	Intrinsic mode functions $C1$ to $C8$ and residual res resulting from the EMD method applied to the wind speed u [9]	13
3.1.	Upper and lower envelopes (blue) using order-statistics filter based estimation, before (a) and after (b) smoothing, and the resulting mean envelope (red) [3]	17
3.2.	The Lena picture, $256 * 256$ pixels	19
3.3.	The 4 modes and the residuum of the Lena picture using the thin plate spline interpolation based BEMD with $SD_{max} = 0.2$	19
3.4.	The 4 modes and the residuum of the Lena picture using the FABEMD with the window width w_4	20
4.1.	Streamwise velocity component of uncontrolled turbulent channel flow at $Re_\tau = 1000$ at $y^+ = 13.5$	23
4.2.	Streamwise turbulence intensity profiles of uncontrolled turbulent channel flow with the FABEMD window-sizing types w_1 (lines) and w_2 (crosses) . .	24
4.3.	Streamwise turbulence intensity profiles of uncontrolled turbulent channel flow with the FABEMD methods w_3 (blue) and w_4 (red)	24
4.4.	Streamwise turbulence intensity profiles of uncontrolled turbulent channel flow with the FABEMD parameters w_1 (lines) and w_3 (dots)	25

4.5. Premultiplied energy spectra of an uncontrolled turbulent channel flow of the streamwise velocity (top), its small-scale signal (center) and large-scale signal (bottom) obtained with w_1 (left) and w_3 (right)	27
4.6. Large-scale (left) and small-scale (right) fluctuations of the streamwise velocity represented in figure 4.1 obtained via w_1 with $n = 7$	28
4.7. Large-scale fluctuations of the streamwise velocity of an uncontrolled (left) and a controlled (right) flow represented in figure 4.1 obtained via w_1 with $n = 7$	29
4.8. Streamwise premultiplied energy spectra with whole velocity signal (top), the small-scale motions (center) or the large-scale motions (bottom) of uncontrolled (left) and controlled (right) turbulent channel flows	30
4.9. Cross-correlation R_{SS} of the small-scale velocity u_{SS} with the inner layer, in the uncontrolled (left) and the controlled (right) channel flow fields, obtained from 5 snapshots of each flow	31
4.10. Cross-correlation R_{LS} of the large-scale velocity u_{LS} with the outer layer, in the uncontrolled (left) and the controlled (right) channel flow fields, computed on 5 snapshots of each field	31
4.11. Streamwise cross-correlation of the large-scales wall friction velocity with the VLSM velocity in the controlled (a) and uncontrolled (b) case, averaged on 16 snapshots of the flow field	33
4.12. Relative difference $\frac{R_{uncontrolled}(\Delta x^+, y^+) - R_{controlled}(\Delta x^+, y^+)}{\max(R_{uncontrolled}(\Delta x^+, y^+))}$ between the correlations of controlled and uncontrolled flow fields	34
4.13. Spanwise cross-correlation of the large-scale wall friction velocity with the VLSM velocity in the controlled (a) and uncontrolled (b) case, averaged on 16 snapshots of the flow field	34
B.1. Modes extracted from the Lena picture via FABEMD with the narrow window methods: w_1 (a) and w_2 (b)	46
B.2. Modes extracted from the Lena picture via FABEMD with the large window methods: w_3 (a) and w_4 (b)	47

List of Tables

3.1. Computational time, mean value, number of maxima and minima, and windowing width for each mode of the decomposition of the Lena picture with the FABEMD method	20
---	----

Bibliography

- [1] H. Abe, H. Kawamura, and H. Choi. Very large-scale structures and their effects on the wall shear-stress fluctuations in a turbulent channel flow up to $re_\tau = 640$. *Journal of fluids engineering*, 126(5):835–843, 2004.
- [2] L. Agostini and M. A. Leschziner. On the influence of outer large-scale structures on near-wall turbulence in channel flow. *Physics of Fluids*, 2014.
- [3] Sharif M. A. Bhuiyan, Reza R. Adhami, and Jesmin F. Khan. Fast and adaptive bidimensional empirical mode decomposition using order-statistics filter based envelope estimation. *EURASIP J. Adv. Signal Process*, 164:1–18, January 2008.
- [4] Jean Duchon. Interpolation des fonctions de deux variables suivant le principe de la flexion des plaques minces. *ESAIM: Mathematical Modelling and Numerical Analysis - Modélisation Mathématique et Analyse Numérique*, 10(R3):5–12, 1976.
- [5] Mohamed Gad-el Hak and Andrew Pollard. *Flow control: fundamentals and practices*. Lecture Notes in Physics Monographs. Springer, Berlin, 1998.
- [6] Davide Gatti and Maurizio Quadrio. Performance losses of drag-reducing spanwise forcing at moderate values of the reynolds number. *Physics of Fluids (1994-present)*, 25(12):125109, 2013.
- [7] M. Guala, S.E. Hommema, and R.J. Adrian. Large-scale and very-large-scale motions in turbulent pipe flow. *J. Fluid Mech.*, 554:521–542, 2006.
- [8] M. R. Head and P. Bandyopadhyay. New aspects of turbulent boundary-layer structure. *Journal of Fluid Mechanics*, 107:297–338, 6 1981.
- [9] Norden E Huang, Zheng Shen, Steven R Long, Manli C Wu, Hsing H Shih, Quanan Zheng, Nai-Chyuan Yen, Chi Chao Tung, and Henry H Liu. The empirical mode decomposition and the hilbert spectrum for nonlinear and non-stationary time series analysis. *Proceedings of the Royal Society of London A: Mathematical, Physical and Engineering Sciences*, 454(1971):903–995, 1998.
- [10] N. Hutchins and Ivan Marusic. Evidence of very long meandering features in the logarithmic region of turbulent boundary layers. *Journal of Fluid Mechanics*, 579:1–28, 5 2007.
- [11] J. Jiménez and A. Pinelli. The autonomous cycle of near-wall turbulence. *J. Fluid Mech.*, 389:335–359, 1999.
- [12] Nobuhide Kasagi and Koji Fukagata. *The FIK Identity and Its Implication for Turbulent Skin Friction Control*. 2006.
- [13] K. C. Kim and R. J. Adrian. Very large scale motion in the outer layer. *Phys. Fluids*, 11(2):417–422, 1999.
- [14] P. Luchini and M. Quadrio. A low-cost parallel implementation of direct numerical simulation of wall turbulence. *J. Comp. Phys.*, 211(2):551–571, 2006.

- [15] Ivan Marusic, Romain Mathis, and Nicholas Hutchins. High reynolds number effects in wall turbulence. In *International Journal of Heat and Fluid Flow* [15].
- [16] Jean Claude Nunes, Yasmina Bouaoune, Éric Deléchelle, Oumar Niang, and Philippe Bunel. Image analysis by bidimensional empirical mode decomposition. *Image and Vision Computing*, 21:1019–1026, 2003.
- [17] Stephen B. Pope. *Turbulent flows*. Cambridge University Press, Cambridge, 2000. Réimpressions (avec des corrections) : 2001, 2003, 2005, 2008, 2010.
- [18] M. Quadrio. Streamwise-traveling waves of spanwise velocity at the wall of a turbulent channel flow. In *iTi Conference on Turbulence, Bertinoro (I), October 12-15, 2008*, 2008.
- [19] S. K. Robinson. Coherent motion in the turbulent boundary layer. *Annual Review of Fluid Mechanics*, 23:601–639, 1991.

Appendix

A. Data processing : from (v, η) to (u, v, w)

Continuity equation :

$$\frac{\partial u}{\partial x} + \frac{\partial v}{\partial y} + \frac{\partial w}{\partial z} = 0$$

Derivative of the velocity in the wavenumber space :

$$\frac{\partial u}{\partial x} = j \hat{u} i_x k_x \text{ with } j^2 = -1$$

Derivate the continuity equation along x :

$$\begin{aligned} \frac{\partial^2 u}{\partial x^2} + \frac{\partial^2 v}{\partial x \partial y} + \frac{\partial^2 w}{\partial x \partial z} &= 0 \\ \frac{\partial^2 u}{\partial x^2} + \frac{\partial^2 v}{\partial x \partial y} + \frac{\partial}{\partial z} \left(\frac{\partial u}{\partial z} - \eta \right) &= 0 \\ -\hat{u}\alpha^2 - \hat{u}\beta^2 - j\hat{\eta}\beta + j\alpha \frac{\partial v}{\partial y} &= 0 \quad \text{with } \alpha = i_x k_x \text{ and } \beta = i_z k_z \\ \hat{u} &= \frac{j(\alpha \partial v / \partial y - \beta \eta)}{k^2} \quad \text{with } k^2 = \alpha^2 + \beta^2 \end{aligned}$$

Derivate the continuity equation along y :

$$\begin{aligned} \frac{\partial^2 u}{\partial x \partial y} + \frac{\partial^2 v}{\partial y^2} + \frac{\partial^2 w}{\partial y \partial z} &= 0 \\ \frac{\partial}{\partial x} \left(\eta + \frac{\partial w}{\partial x} \right) + \frac{\partial^2 v}{\partial z \partial y} + \frac{\partial^2 w}{\partial z^2} &= 0 \\ -\hat{w}\alpha^2 - \hat{w}\beta^2 + j\hat{\eta}\alpha + j\beta \frac{\partial v}{\partial y} &= 0 \quad \text{with } \alpha = i_x k_x \text{ and } \beta = i_z k_z \\ \hat{w} &= \frac{j(\beta \partial v / \partial y + \alpha \eta)}{k^2} \quad \text{with } k^2 = \alpha^2 + \beta^2 \end{aligned}$$

B. FABEMD: Lena picture decomposition with the 4 window-sizing methods

This appendix regroups the modes obtained via fast and adaptive bidimensional empirical mode decomposition applied to the Lena picture 3.2. The four window-sizing methods defined by 3.7 have been used to perform these decompositions.

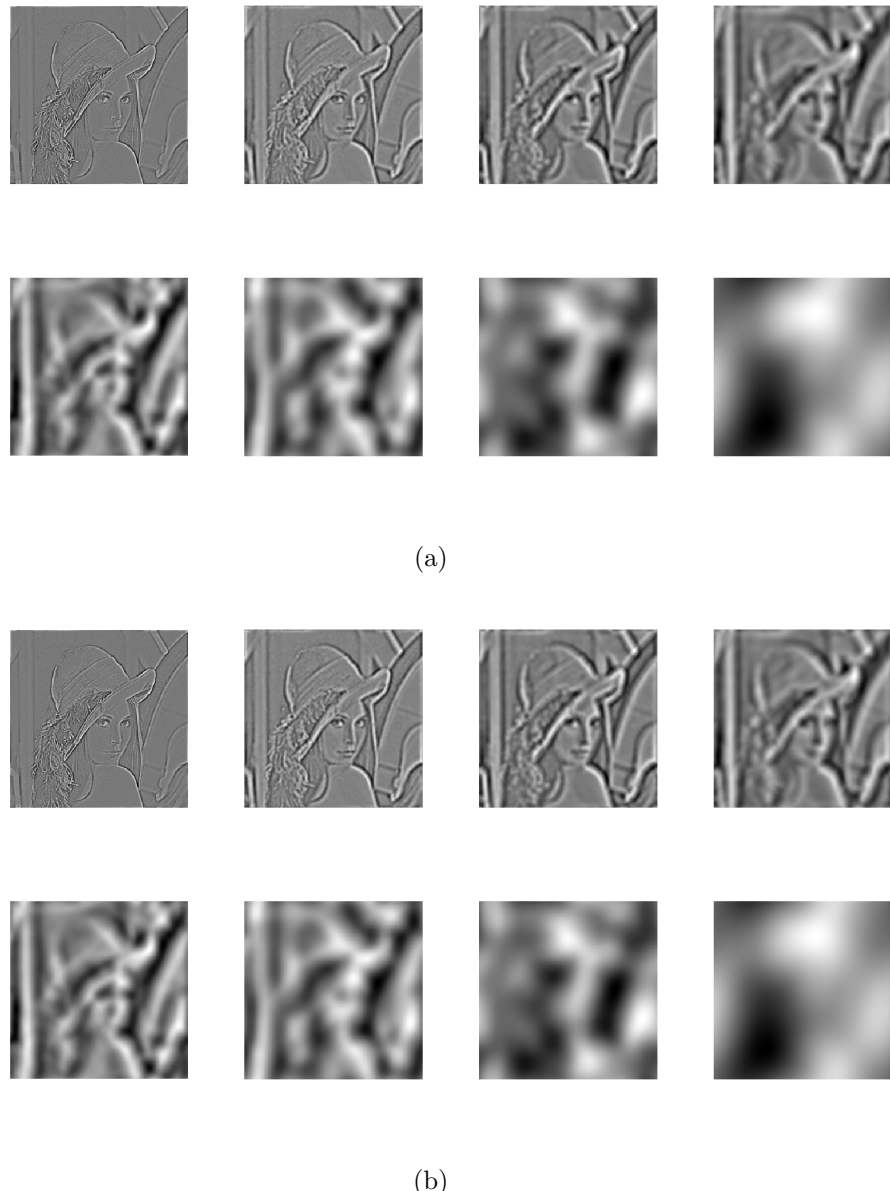


Figure B.1.: Modes extracted from the Lena picture via FABEMD with the narrow window methods: w_1 (a) and w_2 (b)



Figure B.2.: Modes extracted from the Lena picture via FABEMD with the large window methods: w_3 (a) and w_4 (b)